COMPUTATION OF VORTICAL FLOW FIELDS OVER A CLOSE-COUPLED DELTA CANARD-WING CONFIGURATION AND ADJOINT BASED CONFIGURATION OPTIMIZATION

A THESIS SUBMITTED TO
THE GRADUATE SCHOOL OF NATURAL AND APPLIED SCIENCES
OF
MIDDLE EAST TECHNICAL UNIVERSITY

BY

ALP TIKENOĞULLARI

IN PARTIAL FULFILLMENT OF THE REQUIREMENTS
FOR
THE DEGREE OF MASTER OF SCIENCE
IN
AEROSPACE ENGINEERING

FEBRUARY 2022

Approval of the thesis:

COMPUTATION OF VORTICAL FLOW FIELDS OVER A CLOSE-COUPLED DELTA CANARD-WING CONFIGURATION AND ADJOINT BASED CONFIGURATION OPTIMIZATION

submitted by **ALP TIKENOĞULLARI** in partial fulfillment of the requirements for the degree of **Master of Science in Aerospace Engineering Department, Middle East Technical University** by,

Prof. Dr. Halil Kalıpçılar
Dean, Graduate School of **Natural and Applied Sciences** _____

Prof. Dr. Serkan Özgen
Head of Department, **Aerospace Engineering** _____

Prof. Dr. İsmail Hakkı Tuncer
Supervisor, **Aerospace Engineering, METU** _____

Examining Committee Members:

Prof. Dr. Yusuf Özyörük
Aerospace Engineering, METU _____

Prof. Dr. İsmail Hakkı Tuncer
Aerospace Engineering, METU _____

Prof. Dr. Sinan Eyi
Aerospace Engineering, METU _____

Prof. Dr. Hüseyin Nafiz Alemdaroğlu
School of Civil Aviation, Atılım University _____

Prof. Dr. Ünver Kaynak
Aerospace Engineering, Ankara Yıldırım Beyazıt University _____

Date: 10.02.2022

I hereby declare that all information in this document has been obtained and presented in accordance with academic rules and ethical conduct. I also declare that, as required by these rules and conduct, I have fully cited and referenced all material and results that are not original to this work.

Name, Surname: Alp Tikenoğulları

Signature :

ABSTRACT

COMPUTATION OF VORTICAL FLOW FIELDS OVER A CLOSE-COUPLED DELTA CANARD-WING CONFIGURATION AND ADJOINT BASED CONFIGURATION OPTIMIZATION

Tikenoğulları, Alp
M.S., Department of Aerospace Engineering
Supervisor: Prof. Dr. İsmail Hakkı Tuncer

February 2022, 79 pages

This study aims at investigating the vortical flow field over a close-coupled delta canard-wing configuration to understand the vortex interactions and the mechanism of lift enhancement provided by the canard, especially at high angles of attack, and employing an adjoint based configuration optimization to achieve further enhancements in aerodynamic forces. An open-source CFD solver, SU^2 is employed for both flow field computations and adjoint based configuration optimizations. First, flow solutions with SU^2 are verified with solution adaptive grid refinements and turbulence models. The interaction of the canard vortex with the wing vortex, its influence on the vortex breakdown and the lift generated are investigated at different angles of attack. Finally an adjoint based optimization algorithm is developed to locate the optimum position of the canard relative to wing surface. The canard translation is achieved by the rigid motion a free-form deformation box, which encloses the canard. Flow solutions show that the vortex interactions are limited at low-angle-of-attack cases but at moderate and high angle of attacks, the canard vortex enhances the total lift by eliminating the wing vortex breakdown or by pushing the breakdown location further downstream. As the result, 12% and 16% increments in lift are achieved at $\alpha = 20^{\circ}$

and $\alpha = 30^{\circ}$, respectively. The configuration optimization performed at $\alpha = 8.7^{\circ}$ further improves the lift by 1.32%, despite the fact that at such low angles vortex interactions are limited and geometric boundaries further limits the design space. The configuration optimization at $\alpha = 20^{\circ}$, shows that canard's horizontal translation does not have an impact as much as vertical translation on lift improvement. However, closer canard-wing layout provides restoring of burst canard vortex and improves the canard lift.

Keywords: close-coupled canard-wing, delta-wing, canard, aerodynamic optimization, adjoint, vortical flow, SU2

ÖZ

YAKIN İLİŞKİLİ DELTA KANARD-KANAT KONFİGÜRASYONUNDA GİRDAPLI AKIŞ HESAPLAMALARI VE ADJOİNT YÖNTEMİ İLE KONFİGÜRASYON OPTİMİZASYONU

Tikenoğulları, Alp
Yüksek Lisans, Havacılık ve Uzay Mühendisliği Bölümü
Tez Yöneticisi: Prof. Dr. İsmail Hakkı Tuncer

Şubat 2022 , 79 sayfa

Bu çalışmada yakın ilişkili delta kanard-kanat konfigürasyonu, girdap etkileşimlerinin ve özellikle perdövitese yakın yüksek hücum açılarında kaldırma kuvveti artışını sağlayan mekanizmanın anlaşılabilmesi amacıyla incelenmektedir. Akışın incelenmesinin ardından kaldırma kuvvetinde daha yüksek artışlar sağlanabilmesi amacıyla mevcut geometriye adjoint yöntemi kullanan bir gradyan tabanlı optimizasyon yöntemi aracılığıyla konfigürasyon optimizasyonu çalışması uygulanmaktadır. Akış çözümlerinde ve adjoint hesaplamalarında açık kaynaklı HAD çözücüsü olan SU^2 yazılımı kullanılmaktadır. Çalışma öncelikle çözüme bağlı adaptif ağ iyileştirmeleri ve türbülans modellerinin deney sonuçları ile karşılaştırmalarıyla valide edilmektedir. Sonrasında düşük, orta ve yüksek hücum açılarını temsil eden üç farklı hücum açısında akış incelenmekte ve son olarak konfigürasyon optimizasyonu ile kanardın yeniden konumlandırılması sonucu kaldırma kuvvetinde daha yüksek artışlar sağlanmaktadır. Optimum kanard pozisyonunun arandığı çalışmada kanard hareketi kanardı saran bir serbest biçimli deformasyon kutusunun bir bütün olarak hareketiyle sağlanmaktadır.

Akış çözümlerinin incelenmesi sonucunda düşük hücum açılarında girdap etkileşimlerinin sınırlı bir düzeyde olduğu fakat girdap kırınımının etkili olduğu orta ve yüksek hücum açılarında kanard varlığının kırınımı tamamen ortada kaldırması veya en azından geciktirmesi sayesinde kaldırma kuvvetinde önemli artış sağlandığı görülmektedir. Bu artış miktarının $\alpha = 20°$'de $\%12$, $\alpha = 30°$'de ise $\%16$ olması yüksek açılarda kanard etkisinin daha da önem kazandığını göstermektedir. Konfigürasyon optimizasyonu ile kaldırma kuvvetinde daha fazla artış sağlanmaktadır. Her ne kadar düşük hücum açılarında etkileşim kısıtlı olsa ve geometrik sınırlar optimizasyon çalışmasının tasarım uzayını kısıtlıyor olsa da optimize edilen kanard konumuyla birlikte $\alpha = 8.7°$'de $\%1.32$ artış sağlanmaktadır. $\alpha = 20°$ hücum açısında yapılan konfigürasyon optimizasyonu ise bu açıda kanardın yatay eksendeki hareketinin kanat girdabında önemli iyileşmeler sağlayamadığını göstermektedir. Diğer taraftan, kanard ve kanadı daha da yakın ilişkili hale getirmenin kanat akışı üstündeki olumlu basınç gradyanı sayesinde kanard girdap kırınımının onarılması etkisini pekiştirdiği gözlemlenmektedir.

Anahtar Kelimeler: yakın ilişkili kanard-kanat, delta kanat, kanard, aerodinamik optimizasyon, adjoint, girdaplı akış, SU2

To my cousin

ACKNOWLEDGMENTS

I would like to express my sincere gratitude to my supervisor Prof. Dr. İsmail Hakkı Tuncer for his criticism, support and guidance throughout my all M.Sc. progress. I am grateful to him for his valuable advices.

I gratefully acknowledge the supports of RUZGEM (METU Center for Wind Energy) by providing their computational resources of High Performance Computing Laboratory. Also I would like to thank Aeros Inc. for their computational resource support.

I am particularly grateful to Kaan Yutük for his valuable and endless supports through the project. My special thanks are extended to Heyecan Utke Koyuncuoğlu, Tansu Sevine, Hüseyin Can Önel and Ali Ahmed. Their willingness to discuss the theory and the methodology provided crucial improvements to the study. Heyecan and Kaan are more than a friend or a colleague, with whom I will always be grateful for endless discussions all about the human-being.

Special thanks to my close friends Emrecan İnan, Mustafa Alp, Ömer Burak Kınay, Semih Umut Çetin and Sinem Kınay. They are more than brothers and sister to me who have never left me alone for over 10 years. Thanks for all the priceless moments guys!

I owe more than thanks to my family, who have been endlessly supportive and encouraging throughout all my life. Father and brother have always been the ones who I can discuss and learn precious knowledge about the engineering problems. Mother always looked after me with all her kindness, thanks for anything you taught to me and making the life much easier mom! I'm very proud of being a member of such family.

I owe my deepest gratitude to my lovely girlfriend Deniz Sivrioğlu. She has always been by my side and always supported me in both my personal and academic life. Her kindness and love made my life much more meaningful and easier.

Last but the most valuable gratitude goes to my dearest cousin Sevim Deliçay, who lost her battle to cancer in 2019. She was always a wise mentor to me and the biggest supporter throughout my life. Her guidance and advices, not only in professional life, but also in other aspects of life and other fields of interests, shaped my life. As a tribute, I dedicate my thesis to her, rest in peace.

TABLE OF CONTENTS

LIST OF TABLES

TABLES

LIST OF FIGURES

FIGURES

LIST OF ABBREVIATIONS

2D	2 Dimensional
3D	3 Dimensional
RANS	Reynolds-Averaged Navier-Stokes
URANS	Unsteady Reynolds-Averaged Navier-Stokes
DAKOTA	Design Analysis Kit for Optimization and Terascale Applications
JST	Jameson-Schmidt-Turkel scheme
S-A	Spalart-Allmaras
SST	Shear Stress Transport
DDES	Detached Delayed Eddy Simulation
SARC	Spalart-Allmaras with Rotation/Curvature Correction
FVM	Finite Volume Method
FGMRES	Flexible Generalized Minimum Residual
ILU	Incomplete Lower Upper factorization
Tcl	Tool Command Language
NLP	Non-linear Programming
SQP	Sequential Quadratic Programming
BFGS	Broyden-Fletcher-Goldfarb-Shanno
AD	Automatic Differentiation
AoA	Angle of Attack
TSD	Transonic Small Disturbance
VLM	Vortex Lattice Method
NLVLM	Non-Linear Vortex Lattice Method

LIST OF SYMBOLS

C_L	Lift coeficient
$C_{L_{max}}$	Maximum lift coefficient
C_D	Drag coeficient
C_M	Moment coeficient
C_P	Pressure coeficient
α	Angle of attack
L/D	Lift-to-drag ratio
C_{L_α}	$\frac{dC_L}{d\alpha}$, lift curve slope
C_{M_α}	$\frac{dC_M}{d\alpha}$, moment curve slope
x/c	x location, non-dimensionalized by wing root chord
y/b	y location, non-dimensionalized by wing span
U_{axial}	Axial velocity of wing vortex core
U_∞	Freestream velocity
M	Mach Number
Re	Reynolds Number
Pr	Prandtl Number

CHAPTER 1

INTRODUCTION

Combat aircraft are always demanded to be agile and have high maneuverability capability. From WWII to nowadays, agility and maneuverability are the key flight performance parameters for combat aircraft since they can provide competence to overcome counter missile or fighter attacks.

The first response to this demand is given by introducing high-swept delta-wing aircraft. Beginning from the moderate angles of attack, the flow over backward-swept wings with sharp leading edges is separated due to adverse pressure gradient on the leeward side. This separation forms a primary vortex sheet, rolling up over the suction side of wing surface, and a secondary, and in some cases a tertiary, separation vortex sheets in boundary layer region. In figure 1.1, Tu [68] clearly illustrates those counter-rotating vortex sheets and their separation and attachment lines on the wing. Vortex sheets have large axial velocities in vortex core at low and moderate angles of attack due to very low pressure. This low pressure also generates a suction force, as known as vortex lift, on the suction side of wing [25]. This separated sheet forms a stable vortex that can last up to higher angles of attack where the low-swept wings totally stall and lift due to the attached flow is lost. The vortex lift becomes the main lift generation mechanism for slender wings at such high incidences and it enhances the maximum lift capability.

At sufficiently high angle of attack, the vortices suddenly expand due to high swirl level and adverse pressure gradients, the jet-like axial velocity is lost and a low-velocity, wake-like flow downstream is seen [25]. This phenomenon is called as vortex breakdown. Gursul [25] states that there are various sources of disturbances, or instabilities, leading to breakdown of a stable separation vortex sheet, such as shear

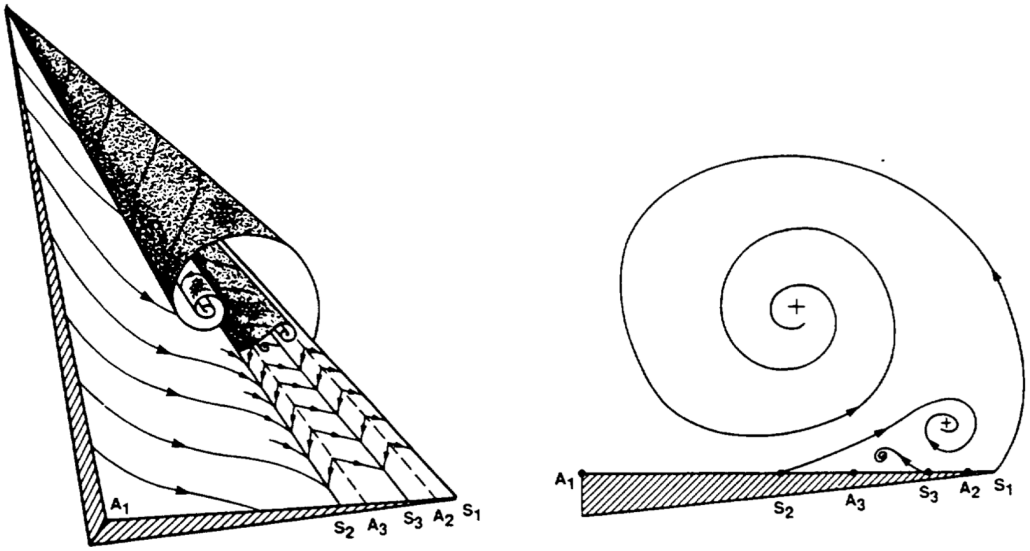

Figure 1.1: Leading edge separation vortex sheets over a delta wing, [68]

layer instabilities, vortex wandering or helical mode instability. Helical mode instability is the main mechanism leading to vortex bursting and a spiral form of breakdown exists as a consequence of this instability. In figure 1.2, helical instability and at the downstream location the burst vortex core is illustrated. As stated above, the main mechanism that influences vortex lift is low pressure and high axial velocity in the vortex core. Vortex breakdown suddenly decreases the magnitude of low pressure in vortex core and thus, it is the dominant flow mechanism responsible for loss of lift. As the angle of attack increase, breakdown location moves upstream to the wing apex and at a certain angle, breakdown occurs suddenly at the wing apex, in other words wing stalls, totally (figure 1.3).

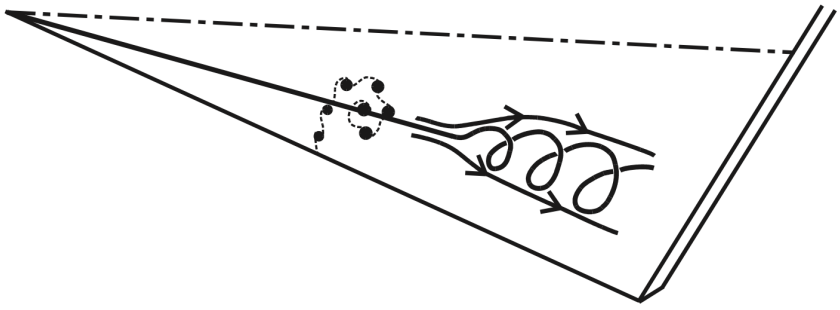

Figure 1.2: Helical mode instability and spiral type of vortex breakdown, [25]

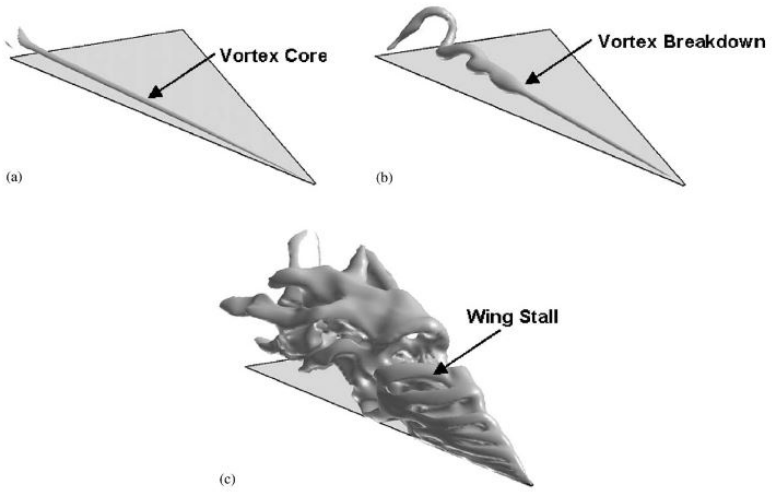

Figure 1.3: Breakdown development as angle of attack increase, [23]

By eliminating, or, at least, delaying the breakdown, high lift performance of delta wings can be enhanced. There are several active and passive control techniques to delay the vortex breakdown and application of close-coupled delta canard-wing configuration is one of those passive control techniques. A close-coupled canard-wing configuration is characterized by two lifting surfaces, namely canard and wing, which are placed sufficiently close to each other so that their leading edge separation vortices favorably influence each other's vortex structure. Mainly, this configuration is used to enhance the jet-like flow behavior of wing vortex core at such high angles of attack where this vortex core is broken down. Bergamnn et al. [4] illustrate the vortex trajectories in figure 1.4 and make the flow morphology more clear. The flow structure over such configuration is characterized by the downwash and upwash effects of canard, which significantly influence the flow over wing, and interactions between canard and wing vortices. By considering the rotation axis of primary leading edge vortices given in figure 1.1, canard implies a downwash effect on the wing's inboard portion which lies within the canard span length. This effect induces the flow, results a decrease in effective angle of attack of wing's inboard portion and delays the vortex formation, if the canard is placed sufficiently close to the wing. On the other hand at the downstream locations of where canard vortex crosses over the wing vortex, canard's upwash effect influences the wing vortex. Moreover, as Yutuk et al. [76] state, although two vortex cores do not entangle, presence of canard vortex provides wing vortex breakdown delay also by preventing wing vortex from its expansion and diffu-

sion. These interactions lead to an improvement in aerodynamic performance of such configuration. Adding a lifting surface in front of the wing also drastically effects the moment characteristics. Canard configuration reduces the longitudinal static stability and it is used to achieve a more agile, high maneuver aircraft.

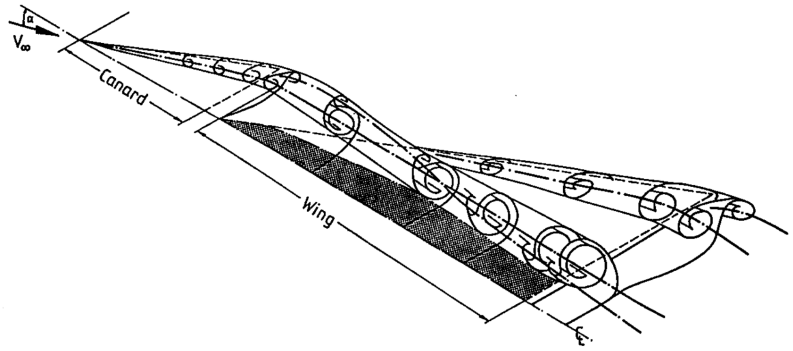

Figure 1.4: Schematic of vortex trajectories over close-coupled delta canard-wing configuration, [4]

Canard position and deflection angle can dramatically change the aerodynamic characteristics. Studies show that the maximum lift increment is achieved when the canard is positioned at the upward of wing chord-line and as close to wing as possible, while positioning the canard at the downward of wing chord-line may cause unfavorable vortex formations on the pressure side of wing. In addition, overall lift is almost independent from canard deflection angle. Positive canard deflection results an increase in canard lift, however, it also increases the downwash of canard wake. Due to increasing downwash of canard's wake, wing's effective angle of attack decreases and consequently lift generated by wing surface decreases. This reduction on wing lift balances the increase in canard lift and as the result, total lift becomes almost independent from canard deflection. On the other hand, effects of canard deflection on pitching moment are significant, increasing canard lift remarkably influences the pitch-up moment. Canard's horizontal positioning also affects the pitch-up moment characteristics since the moment arm between canard lift and neutral point is determined by canard's horizontal position.

The high swept wing, or delta wing, concept dates back to early 1930s. The first successful application of delta wing is accomplished by Lippisch [44]. After the WWII,

Lippisch's delta wing aircraft is moved to United States and extensive investigations are conducted on it. In 1946, Wilson et al. [75] changes Lippisch's rounded leading edges with sharp leading edges and demonstrate the potential of delta wings on increasing performance in $C_{L_{max}}$. Therefore, Wilson et al. provide a new concept, which is well-known today, of which separation induced and highly stable leading-edge vortex flow with its associated vortex lift. The effects of leading-edge vortices are first clarified by Polhamus [56, 57]. Leading edge suction analogy is studied extensively after Polhamus. Lamar [41] publishes an extension of a current analogy to predict the effect of side edge vortices.

1.1 Experimental Studies on Close-Coupled Delta Canard-Wing Configurations

In order to improve the stall characteristics of a delta-wing aircraft, the studies show that lift capability of slender, i.e. low aspect ratio, delta wings may be enhanced by the vortex interaction effects. The studies conducted in 1960's and early 1970's put the first results in literature and revealed some remarkable results which were contrary to general knowledge during those days. These results show that even moderate aspect-ratio and less-swept wings can also generate high lifts at extreme angles of attack by creating favorable vortex interactions. One such modification is placing a canard just ahead of the wing. Since there is a small distance between the canard and wing, such configuration is named as close-coupled canard-wing configuration. The aerodynamics and the mechanism that result lift enhancement of close-coupled delta canard-wing configurations have been studied both experimentally and numerically for many years. First study for such configuration is conducted by Behrbohm [2] and the results are applied to the Saab Viggen successfully. Behrbohm carries out a parametric study on a model having a fuselage and a close-coupled delta canard and wing surfaces. He results that canard suppresses the formation of wing vortex at the wing apex, on the other hand, at downstream it enhances the already-formed wing vortices. As the result, lift is increased up to 65% on final design, compared to wing-alone configuration, while the wing loading is almost identical. Behrbohm also reports that application of the canard enhances trim requirements. The wing trailing edge should

be deflected downward to balance the pitch-up behavior resulting from the canard lift and this deflection increases wing lift.

Lacey [38, 39, 40] conducts an exhaustive study on close-coupled delta canard-wing configuration, including the investigations on canard-wing vortex interactions; tail interferences, effects of canard 's shape and position on lift, drag and moment forces. Some remarkable observations are, increasing canard sweep strengthens the canard vortex and hence increases $C_{L_{max}}$. Increasing canard size results an increase in C_L. Moving the canard upward increases the vortex interaction and favorably affects the stall behavior, while moving the canard further away from the wing reduces this interaction, and therefore upper canard being closer to wing is the optimum location for all four different canard shapes concerned in Lacey's study. He also reports that moving the canard further away and increasing canard deflection increases pitching moment.

Meanwhile, experimental studies on close-coupled canard-wing configuration continues also at the Langley Research Center, pioneered by McKinney, Dollyhigh, Gloss and their colleagues [20, 19, 21, 52]. Gloss and Mckinney [20] conducts an experiment at Mach numbers 0.7 and 0.9, mainly concerning the effect of canard-wing interference on lift force. They test different vertical and longitudinal canard positions coupled with different wing sweeps. They report that downwash effect causes a decrease in wing lift for the angles of attack smaller than 16°, but overall lift is higher than canard-off configuration, due to additional lift coming from canard. Above $\alpha = 16^\circ$, wing vortex breakdown is delayed and therefore wing lift is also increased. They report that canard deflection does not change overall lift since the lift increase on canard is balanced with the lift decrease on wing due to canard's increased downwash effect. Another study conducted by Gloss [19] uses the same experimental model with the previous study, but this time a new strake-canard geometry and a different cambered and twisted wing are added into the study and longitudinal stability characteristics are also evaluated. Due to this study, the canard positioned above the wing plane produces the highest $C_{L_{max}}$, except the strake-canard configuration; adding strake on the canard provides larger lift improvements to the lower canard, rather then high canard configuration. High canard position also provides the most linear C_M curve, since the nonlinearities in the pitching moment is a result of burst

vortex. He also states that wing camber and twist has no effect on the lift. In [21], Gloss provides detailed wing chord-wise pressure distribution plots that clearly show the abrupt pressure changes due to wing vortex breakdown. He states that canard downwash reduces the lift at wing stations immediately behind the canard and the same mechanism increases the lift at outboard sections of wing. Paulson et al. [52] analyzes the enhanced lift capability of close-coupled canard-wing configuration also for enhancing the take-off and landing performance of Vertical or Short Take-off and Landing (V/STOL) combat aircraft. It is concluded that canard-wing configuration performs well in transition flight, which is needed for STOL capable aircraft.

Calarese [9] provides a detailed flow field evaluation in his study. Both local axial and lateral velocity plots are provided, which are the key data to analyze the vortex behavior on wing in his study. Reynolds stresses and turbulence intensity are also obtained, unlike the previous studies, as he states. He also applies air injection at the wing leading edge to enhance the wing vortex and increase the lift. In another study [10], Calarese assesses coplanar-canard-wing and high-canard arrangements in terms of lift and lift-to-drag (L/D) ratio. He reports that coplanar configuration can provide only 2% increase in L/D at $\alpha = 10^\circ$ and 4% at $\alpha = 16^\circ$ compared to canard-off configuration, while the high-canard configuration provides 12% higher L/D at both angles of attack compared to coplanar configuration.

Er-El and Seginer [15] investigate canard shape and position. They report that wing-narrow-canard (75° swept canard in their case) interference is controlled by strong leading-edge vortex interactions, while the wing-wide-canard (56° swept canard) interference is controlled by the flow field deflection generated by canard. So, higher swept canard is preferred for strong vortex interactions. In their study canard-off (or wing-alone) case has almost constant C_M vs. α curve, on the other hand application of canard changes C_M vs. α curve to positive slope and increasing longitudinal separation of canard and wing increases C_M by increasing the moment arm. In [16], Er-El and Seginer use the same configurations and investigate vortex trajectories and breakdown in more detailed. Span-wise and vertical components of leading edge vortex trajectories at different angles of attack are plotted for both canard-on and canard-off configurations and their vortex breakdown locations are shown in the paper. Within the accuracy of Schlieren picture, they can not observe any significant differences

between the vortex breakdown locations of studied three canard-wing configurations. However, vortex trajectories differ significantly. In his next study [14] Er-El provides detailed span-wise C_P distribution plots at several sections over the wing and evaluates the effect of wing-canard interference on pressure field.

In Technical University of Braunschweig a series of experiments are conducted on vortical flows on delta wings and canard-wing configurations. Hummel put together his observations on slender delta wings, double delta wings and canard-wing configurations in [32]. For canard-wing configuration, he observe such lower suction peaks in front part of the wing, supporting the previous observations that canard downwash reduces wing's effective angle of attack. It is also observed that canard vortex breaks down at $\alpha > 12^\circ$ but due to wing induced pressure gradients, canard vortices are restored to a non-burst state in the wing leading edge region. The complete flow field study of this configuration is published in [50]. The primary, secondary and tertiary vortices are plotted at certain section over the wing by total pressure and dynamic pressure isobars, and those isobar plots provide a detailed explanation of mechanisms of vortex interactions. Hummel and Oelker repeats a similar study on canard-wing configuration of International Vortex Flow Experiment [33]. Observations in this study are similar to [50]. Both experiments are at relatively small angles of attack where vortex breakdown does not occur and at such angles of attack canard and wing vortex systems remain separate up to wing trailing edge. In both studies authors observe that canard's downwash suppress flow separation in the front and inner parts of wing, while canard's upwash supports separation in outer portions of wing. In 1991, Bergmann, Hummel and Oelker publish another study [4], using a similar canard-wing geometry but with a different cylindrical fuselage. Authors investigate higher angles of attack, up to $\alpha = 40^\circ$, and unsymmetrical flow characteristics on canard-wing configuration at different sideslip angles. Flow structure is given by pressure distribution plots over canard and wing. In 2001, Bergmann and Hummel publish a study in which the effect of canard position is investigated [3]. The same geometry with [4] is used in this study but this time with different vertical positions and different setting angles of canard. Similar to previous studies, Bergmann et al. observe that overall lift is almost independent of the canard setting angle but $C_{L_{max}}$ considerably reduces with increasing setting angle, while nose-up pitch moment increases

with increasing setting angle. Those observations are common for all three positions, considered in this study, of the canard.

Ponton et al. [58] provide detailed evaluations of decalage angle, which is the angle between canard and wing chord lines, and canard position at a wide range of angle of attack. They obtain that negative decalage angles provide stabilizing pitch down moment, while increasing it increases the pitch up moment. They also report that there is a strong relation between decalage and incidence angles in terms of getting favorable canard influence on C_L and summarize the relation between decalage angle, incidence and percentage C_L change in a contour plot. For all angles of attack and canard positions given in the study, the maximum increase in C_L is provided by the decalage angles around 0° but in negative region.

Howard and Kersh also publish their observations on the effect of canard deflection on lift enhancement in their paper [29]. They report that at $\alpha = 22^\circ$ maximum lift enhancement due to canard deflection is about 5% at the canard deflection of $+7^\circ$. On the other hand, at $\alpha = 34^\circ$, maximum lift enhancement is reached with the canard deflection of -7°. Howard and O'Leary [30, 31] extended the previous study by examining the flow field behavior of close-coupled canard-wing configuration. The model examined in this paper has 7° canard deflection angle and set at $\alpha = 22^\circ$. Flow field is examined by plotting cross-plane streamlines, velocity vectors and pressure loss contours at several sections on canard and wing.

1.2 Numerical Studies on Close-Coupled Delta Canard-Wing Configurations

With the increasing attention to delta canard-wing configurations, studies which aim predicting flow behavior on such configurations by numerically emerged as well as the experimental studies. First numerical studies are based on analytical solutions like drag prediction calculations and Polhamus' leading edge suction analogy method. Goldstein and Combs [22] use an analytical approach to calculate trim drag for a canard and aft tail configuration. They obtain that canard configuration has a potential of reducing trim drag, increasing the L/D throughout the flight range. Moreover, floated canards can raise the maximum trimmed L/D and reduce the drag at high lift

coefficients even more. Butler [8] calculates the induced drag of canard-wing and wing-tail configurations based on Prandtl's biplane theory. His calculations show that additional induced circulation effect act to reduce the drag. This effect is small for wing-tail configuration but significant for the canard-wing layout.

In the study published by Campbell et al. [11], theoretic calculations are based on Polhamus' leading edge suction analogy [57] for simple delta wings and and extended version of this analogy [42] for multiple lifting surfaces like canard-wing configurations. These numerical methods well predict C_L curves and drag polars for canard-off and canard-on configurations up to stall angles, however deviate at near- and post-stall regimes. Hale et al. [26] develop a semi-empirical potential flow based formulation in which the vortex sheets are added. In order to simulate vortex bursting, vortices are modeled by the combination of horseshoe vortices and burst vortex sheets, where the wing and burst vortex vectors are determined by experiments. The formulation represents both potential lift dominated low angles of attack and vortex lift dominated high angles of attack. But this methodology requires extensive experiments to locate the horseshoe vortices and burst vortex sheet, which remains as a disadvantage.

Due to being low-cost, potential flow based methods such as Vortex Lattice Method (VLM) or Transonic Small Disturbance (TSD) method are commonly used to predict flow behavior on such delta wing configurations, especially in 70's and 80's, and regarded as having a potential to be used as a "design by analysis" process employed during the preliminary design [62]. Henderson evaluates potential flow and potential plus vortex methods by comparing them to experiment at different canard positions [27]. He reports that potential plus vortex solutions works well for mid- and high-canard configurations, C_L and C_D curves fit to experiment, while potential flow solutions fit better at low-canard positions. Investigation of aerodynamic characteristics reveals some observations similar to previous studies. Canard improves the trimmed lift capability, reduces the trimmed and wave drags; while at low angles of attack lift increment by canard is balanced by lift loss on wing due to the decreased effective angle of attack, at $\alpha > 8^\circ$ total lift enhancement is significant; and while low-and mid-canard increase the longitudinal stability, high-canard results a pitch-up moment.

Kandil et al. [36] apply a Non-Linear Vortex Lattice Method (NLVLM) to the canard-wing configuration by accounting viscous effect by artificial viscosity terms. Qualitative and quantitative comparisons of vortex lines, normal-force coefficient vs. α and center of pressure location vs. α curves show that the numerical predictions are in a good agreement with Behrbohm's experimental work. Stoll and Koenig [64] use higher-order panel method and VLM. They observe that panel method predictions are valid only at small angles of attack, its lift prediction deviates 10% at $\alpha = 13.5^{\circ}$. On the other hand VLM has a good lift and moment accuracy up to $\alpha = 20^{\circ}$, actually where the breakdown effects become significant. They also obtain notable observations on vortex interactions. Canard delays the wing stall even if the canard is completely stalled and it results a 34% increase in total $C_{L_{max}}$, although canard adds 15% more lifting area, and pitch control inputs are effective up to stall angle. Rom and Gordon [61] employ NLVM to evaluate the effect canard position and deflection angle. Their observations are, canard's vertical position has a very limited effect, while canard's horizontal position affects both lift and pitch-up moment. Canard deflection angle has no effect on overall lift but it strongly affects pitching moment, pressure distribution and L/D at low angles of attack. In another paper of Rom et al. [62], extend their work on different wing-canard models. Gordon [24] also states that integrated force coefficient start diverging from measurements at $\alpha \approx 10^{\circ}$ due to errors on C_P calculations. All the authors' comparisons of numerical predictions to experimental measurements show the weaknesses of the method. Since the method is based on inviscid flow assumption, friction drag can not be predicted in calculations, and also calculated pressure distribution differs from measurement which leads to mis-predictions of moment coefficient. Mis-predictions at high angles of attack, mentioned by authors, are also due to viscous nature of vortex breakdown mechanism.

TSD method, on the other hand, can not be employed at high angles of attack due to its small disturbance assumption but emerges as an important method for transonic regimes, where subsonic potential flow formulations can not be used [1]. Agrell et al. [1] use TSD and linear panel methods to examine elevon deflections and evaluate aerodynamic derivatives at mach number range between 0.2 and 2.0. Although both methods over-predict aerodynamic derivatives, C_{L_α} and C_{M_α}, at transonic regime, for

elevon deflection case, they represent good tendency of change with mach number. Panel method is insufficient for mach numbers between 0.9-1.2. So authors present the TSD method as an important complementary tool to panel method as the later is insufficient in mach number range $0.9 < M < 1.2$.

The previous discussed models, based on potential flow theory, require the vortex sheets to be hand fitted, it require an extensive effort to represent the vortices correctly. On the other Euler equations allow the vortex sheets to be captured automatically [17]. Therefore with advancing computer technology, Euler simulations become more suitable for numeric predictions of such configurations. Eriksson and Rizzi conduct a steady state Euler simulation at 0.7 Mach and $\alpha = 10^{\circ}$ [17]. The paper evaluates total pressure loss and mach contours and also velocity vectors, C_P distribution plots and integrated C_L and C_D values. Contour plots give a qualitative assessment, while C_L and C_D values are used to a quantitative comparison to measured data. The Euler solutions predict C_L value of single delta wing as $C_L = 0.554$, while in experiment $C_L = 0.53$ is measured. Lift coefficients are in good agreement with an error of 4.5%. Longo and Das [45, 13] conduct an extensive study to compare velocities, pressures and loss of total pressures, breakdown location with canard-on and canard-off configurations. They report that strength of wing leading edge vortex is reduced due to addition of canard, and it leads to reduction in the loss of total pressure, compared to canard-off case. They also investigate the breakdown location by plotting the dimensionless axial velocity value, U_{axial}/U_{∞}, throughout the wing. Two saddle points, representing flow reversal and vortex bursting points are shown in those dimensionless axial velocity plots. Also the shift of breakdown location with respect to angle of attack is given and it is a good comparison between inviscid calculations and experimental measurements to show the viscous effects on breakdown phenomenon. Malfa et al. publish a paper [46] which evaluates the inviscid and viscous effects on delta wings. They report that since the primary vortices are mainly inviscid but secondary and tertiary vortices occur due to viscous effects, Euler simulations can only capture the primary vortices and do not resolve the others. Without viscous effects, Euler methods predict a suction peak much higher than the real case. Therefore, numerical artificial viscosity terms are employed in Euler equations and in this paper control coefficients of these terms are discussed in detail.

In order to resolve viscous effect, which is shown that it has a crucial effect on the mechanism of formation and bursting of vortices, Euler equations are not sufficient, Navier-Stokes equations are needed to be solved including viscous terms. On the other hand, it is more expensive than all the other methods discussed above. Navier-Stokes simulations become being affordable in 90's, with the advances in computer technology, and from then on, they emerge as the most commonly used numerical methods employed in such problems. Tu publishes a series of papers in which he evaluates the vortex interactions and effects of canard position and deflection angles, by employing thin-layer Navier-Stokes equations [66, 65, 67]. The equations are solved at transonic regime, $M = 0.85 - 0.9$, and at relatively low angles of attack, up to $\alpha = 14^{\circ}$. His findings are similar to previous studies but there are some notable observations. First of all, viscous secondary vortex is clearly resolved by the method. The numerical method predicts that vortex burst occurs at $\alpha = 12.38^{\circ}$, Gloss and Washburn reported that it occurred approximately at $\alpha = 13^{\circ}$, which results a good agreement. Drag polar curves of canard-on and canard-off cases cross-over at a certain angle of attack, and it shows the potential of canard configuration for high L/D. He reports that, at those angles of attack, canard deflection can cause unfavorable vortex formations on wing lower surface. He also observes that canard position causes significant differences in lift curve at $\alpha > 4^{\circ}$ and high canard configuration provides lift increase and drag reduction. Tuncer et al. [69] conduct a numerical study based on the experiments done by Bergmann et al [4]. They compare the pressure distributions and vortex breakdown locations of canard-on and canard-off configurations at $\alpha = 20^{\circ},\ 24.2^{\circ},\ 30^{\circ}$ at zero sideslip. It is observed that resolving the strong interaction between canard and wing vortices is a challenging problem. They reached reasonable agreements for canard-on case only at $\alpha = 20^{\circ}$ and the solutions differs from measurements at higher angles of attack, especially in the region where breakdown occurs.

Ghoreyshi et al. [18] employ two different CFD solvers using SA, SARC and DDES with SARC turbulence models for simulations of X-31 aircraft model. The numerical solutions provide a detailed investigation of flow field. It is reported that vortex breakdown causes very nonlinear pitching moment behavior because of the nonlinear behavior of flow behind the vortex breakdown and since the moment reference

point is close to aircraft neutral point, C_M is very sensitive to differences in numerical algorithms and solvers. Assessment of turbulence models show that SA model fails to predict the vortex breakdown and its effects due to the diffusive nature of the model when the vortex breakdown occurs. Chen et al. apply DDES method based on S-A turbulence mode to canard-wing configuration in sideslip [12]. They observe unusual rolling moments due to sideslip and it leads abrupt loss of rolling stability at post-stall regime. Canard-wing configuration reveals different roll stability characteristics at different angles of attack, at $\alpha = 10^\circ$ model is in lateral stable condition, at $\alpha = 20^\circ$ rolling moment fluctuates around zero, and at $\alpha = 30^\circ$ significant positive rolling moment is generated with increasing sideslip. Using the same aircraft model and numerical methods, Qin et al. [59] investigate the canard-wing interference in static ground effect. They report that with the ride height decrease, lift, drag, nose-down pitching moment and L/D increase nonlinearly. Those observations contribute to understand the aerodynamic performance of such configurations in take-off and landing phases.

Hitzel and Osterhuber [28] investigate the effect of adding leading-edge root extensions between canard and wing on the enhancement of maneuverability of Eurofighter Typhoon aircraft. They employ unsteady RANS (URANS) equations coupled with $k - \omega$ turbulence model. They reach strong, stable vortices which enhance the maneuverability and overcome the rolling-moment instabilities of previous design.

Wibowo et al. [72, 73, 60, 71] conduct extensive numerical studies on different aircraft models and support their observations with water tunnel tests. In the paper [72], flow over a Russian SU-30 aircraft model is solved by RANS equations coupled with $k-\omega$ turbulence model. The effect of canard deflection angle to improve wing stall is examined. They obtain that negative canard deflection in range of $20^\circ - 40^\circ$ improves the stall characteristics significantly, stall angle is increased form approximately 45° to 50°. Furthermore, the deflection results a smoother post-stall lift characteristics, a significant portion of lift can be preserved up to $\alpha = 80^\circ$ [60] In another paper, Wibowo et al. [73] investigate the effect of canard position by employing DDES method. Results are similar to previous studies, canard positioned closer to wing and above the wing chord line gives the highest lift increment. They report that lift increase up to $5\% - 12.1\%$ is provided. In their most recent studies, Wibowo et al. [71] compare

the aerodynamic performances of Russian SU-30, Chinese J-10 and European EF-T aircraft models.

Yutuk et al [76] publish a study recently, based on Bergmann's [4] experiment. RANS equations are employed in the study and coupled with Menter's $k-\omega$ SST turbulence model. The flow field and vortex interactions are evaluated in detail, by providing surface pressure distributions, total pressure loss contours, vortex core trajectories, and q-criterion iso-surfaces. They concluded their study with some remarkable observations. Thanks to advanced numerical methods and employed grid-refinement technique, this study achieves a better agreement with experimental measurements in comparison to previous numerical studies published in late nineties. Vortex breakdown does not occur up to $\alpha = 20^{\circ}$ and it is moved downstream on wing by 60% of wing chord at $\alpha = 30^{\circ}$. As the result, 12% and 16% lift increment is provided at $\alpha = 20^{\circ}$ and $\alpha = 30^{\circ}$, respectively.

1.3 Gradient-based Optimization with Adjoint Method

Aerodynamic design optimization is one of the key parts of an aircraft design process in order to maximize its aerodynamic performance under certain conditions. Although there are many techniques in literature, gradient-based methods are the most commonly used optimization techniques in aerodynamic design optimization. The goal is to minimize an objective (or cost) function in the solution set which is limited by the constraints. In order to reach the minimum point, gradient-based methods require gradient or sensitivity calculations, which means that derivative of objective function with respect to design variables has to be calculated. There are different methods for evaluating the gradients. A common way is to apply small perturbations on each design variable and calculate the change in objective function, which is called finite differencing method. Since the flow field should be re-evaluated for the change of objective function for each design variable change, the problem becomes more and more costly with increasing number of design variables. And, aerodynamic design optimization problems are typical cases having such high numbers of design variables. The adjoint method provides an efficient way of gradient calculation of objective function with respect to many design variables [53], and therefore it has

gained popularity in aerodynamic design optimization applications in recent years. The adjoint equations are implemented into solvers by two different techniques, continuous and discrete methods. In continuous adjoint method, first, adjoint equations are implemented into governing equations and then they are discretized. On the other hand, in discrete method, governing equations are discretized and then discrete adjoint equations are implemented.

The adjoint method is based on the control theory [43] and Pironneau [54, 55] is the first one who apply this methodology in fluid problems, to incompressible Euler equations. Jameson [34] introduced the sensitivity analysis procedure for inviscid compressible flows.

Although first implementations of discrete approach dates back to 1982 [7], complexity of this approach had a limitation. Jameson [35] states that complexity of the discrete adjoint formulation is proportional to n^7. However, the advances in automatic differentiation (AD) in last years, made the discrete approach more affordable.

The Free-Form Deformation (FFD) box technique is a widely-used method that is used in aerodynamic shape optimization problem to deform the shapes. The idea is enclosing the geometry to be deformed by a simple lattice structure, defining each node on the structure as control points and controlling the deformation of aerodynamic shape by moving those control points along determined degrees of freedom. In this method gradients are calculated by projection of sensitivity values on to the each control point. As the result, gradients for each control points (or design variables) are obtained.

1.4 Objectives of the Study

This study aims at understanding the vortical flow behavior over a close-coupled canard-wing configuration, effect of canard on delaying the wing vortex breakdown, its consequent effects on aerodynamic performance and performing a layout optimization on a close-coupled canard-wing configuration by using an adjoint-based optimization method. The open-source CFD software SU^2 is employed for the flow and the adjoint solutions on solution adaptive grids. Fully turbulent viscous flow fields

are evaluated by SU^2 solver employing the RANS equations at three different angles, representing low-, moderate- and high-angle-of-attack cases. The baseline configurations of this study are taken from the experimental studies conducted in Technical University of Braunschweig [4, 50]. The vortical flow solutions at high angles of attack are first verified, flow fields and vortex interactions at different angles of attack is investigated. Finally, a configuration optimization is performed. The gradient based optimization process is driven by the open-source optimization software DAKOTA. C_L is chosen as the objective function to maximize, while the vertical and the horizontal location of canard are taken as the design variables.

CHAPTER 2

METHODOLOGY

In this study, the main objectives are to understand the vortical flow behavior over a close-coupled delta canard-wing configuration at different angles of attack and develop an optimization procedure to improve the lift coefficient, C_L, of a such configuration at a given condition. Optimization process focuses on canard's vertical and horizontal position. Geometric boundaries are the limits of design space. The flow field is solved by RANS equations and gradient vectors are obtained by employing the adjoint solution on those solutions. Both flow solutions and adjoint calculations are handled by SU^2.

This chapter begins with an overview of the flow solver SU^2. It is followed by the details of flow field modeling, including governing (Reynolds-Averaged Navier-Stokes, RANS) equations, turbulence modeling, boundary conditions and solver setup in 2.1. Then, the computational grid generation method is introduced in section 2.2 and optimization framework is explained in 2.3. The gradient-based optimization method, including the adjoint based sensitivity and gradient evaluations, hessian approximation and optimization algorithm are described in subsection 2.4.

2.1 RANS Solver: SU^2

In this study an open source flow solver, SU^2, is employed for fluid flow simulations. The solver was initially developed in the Aerospace Design Laboratory of Stanford University, and now still being developed by a world-wide developer community. SU^2 is a node-based finite volume solver using unstructured grids. The governing equations are discretized based on finite volume method in a node-based

order. The solver is capable of describing the flow by inviscid Euler equations, or viscous Navier-Stokes equations. Viscous Navier-Stokes equations can be employed either as time-dependent or steady-state and viscous terms are evaluated by several turbulence modeling options, including S-A, $k-\omega$ SST, hybrid RANS/LES.

2.1.1 Governing Equations

Navier-Stokes equations are actually a set of PDEs that represent the physical modeling of conservation of mass, momentum and energy. The integral form of the governing equations is as following

$$\frac{\partial}{\partial t}\int_{\Omega} U d\Omega + \oint_{S}\left(\vec{F}_c(U) - \vec{F}_v(U)\right).\vec{n}ds = 0 \tag{2.1}$$

where U stands for the flow variables vector in conservative form, $\vec{F}_c(U)$ and $\vec{F}_v(U)$ are the convective and viscous flux terms, relatively. Surface integral represents the integral over the control surface and volume integral over the Ω represents the integration over control volume. In the employed flow solver, SU^2, governing equations are discretized by using a finite volume method. In spatial discretization, a dual grid method is used in which control volumes are constructed using a median-dual, vertex based scheme.

Considering a 3-dimensional problem, vectors of flow variables, convective and viscous fluxes are defined as,

$$U = \begin{bmatrix} \rho \\ \rho v_x \\ \rho v_y \\ \rho v_z \\ \rho E \end{bmatrix} \tag{2.2}$$

where ρ is the density, v_x, v_y and v_z are velocity components and E is the total energy

per unit mass. Convective fluxes have also three components,

$$\vec{F}_c(U) = \vec{F}_{c_x}(U) + \vec{F}_{c_y}(U) + \vec{F}_{c_z}(U) \tag{2.3}$$

$$\vec{F}_{c_x} = \begin{bmatrix} \rho v_x \\ \rho v_x^2 + p \\ \rho v_x v_y \\ \rho v_x v_z \\ \rho v_x H \end{bmatrix}, \quad \vec{F}_{c_y} = \begin{bmatrix} \rho v_y \\ \rho v_x v_y \\ \rho v_y^2 + p \\ \rho v_y v_z \\ \rho v_y H \end{bmatrix}, \quad \vec{F}_{c_z} = \begin{bmatrix} \rho v_z \\ \rho v_x v_z \\ \rho v_y v_z \\ \rho v_z^2 + p \\ \rho v_z H \end{bmatrix} \tag{2.4}$$

where p is static pressure and H is the fluid enthalpy which is $H = E + \frac{p}{\rho}$.

The viscous fluxes, on the other hand, can be written as follows,

$$\vec{F}_{v_x} = \begin{bmatrix} . \\ \tau_{xx} \\ \tau_{xy} \\ \tau_{xz} \\ \Theta_x \end{bmatrix}, \quad \vec{F}_{v_y} = \begin{bmatrix} . \\ \tau_{xy} \\ \tau_{yy} \\ \tau_{yz} \\ \Theta_y \end{bmatrix}, \quad \vec{F}_{v_z} = \begin{bmatrix} . \\ \tau_{xz} \\ \tau_{yz} \\ \tau_{zz} \\ \Theta_z \end{bmatrix} \tag{2.5}$$

Pressure forces and viscous forces create normal and shear stresses on the surface. Those stress terms are denoted by τ_{ij} where τ_{xx}, τ_{yy} and τ_{zz} represent normal stresses, while τ_{xy}, τ_{xz}, τ_{yz} represent shear stresses, and they form a symmetric stress tensor, i.e. $\tau_{ij} = \tau_{ji}$, which can be written as,

$$\bar{\bar{\tau}} = \begin{bmatrix} \tau_{xx} & \tau_{xy} & \tau_{xz} \\ \tau_{yx} & \tau_{yy} & \tau_{yz} \\ \tau_{zx} & \tau_{zy} & \tau_{zz} \end{bmatrix} \tag{2.6}$$

The viscous stresses can be written as

$$\tau_{ij} = \mu_{tot} \left(\frac{\partial v_i}{\partial j} + \frac{\partial v_j}{\partial i} - \frac{2}{3} \delta_{ij} \nabla \cdot \vec{v} \right) \tag{2.7}$$

where $(\nabla \cdot \vec{v})$ is divergence of the velocity, $\delta_{i,j}$ is the Kronecker delta function, and $\mu_{tot} = \mu_{dynamic} + \mu_{turbulent}$. Here, $\mu_{dynamic}$ is assumed to satisfy Sutherland's Law and $\mu_{turbulent}$ is calculated by using turbulence models.

In equation 2.5, Θ represents the work and heat added on the system, where net work done on the element is

$$\frac{DW}{Dt} = \nabla \cdot (\vec{v} \cdot \tau_{ij}) \tag{2.8}$$

and the heat added to the fluid is given by

$$\frac{DQ}{Dt} = \mu^*_{tot} C_p \nabla T \tag{2.9}$$

therefore the three components of Θ are,

$$\begin{aligned}
\Theta_x &= (v_x\tau_{xx} + v_y\tau_{xy} + v_z\tau_{xz}) + \mu^*_{tot} C_p \frac{\partial T}{\partial x} \\
\Theta_y &= (v_x\tau_{yx} + v_y\tau_{yy} + v_z\tau_{yz}) + \mu^*_{tot} C_p \frac{\partial T}{\partial y} \\
\Theta_z &= (v_x\tau_{zx} + v_y\tau_{zy} + v_z\tau_{zz}) + \mu^*_{tot} C_p \frac{\partial T}{\partial z}
\end{aligned} \tag{2.10}$$

where C_p is the specific heat at constant pressure and $\mu^*_{tot} = \frac{\mu_{dynamic}}{Pr_{dynamic}} + \frac{\mu_{turbulent}}{Pr_{turbulent}}$.

2.1.2 Turbulence Modeling

In Reynolds equations, Reynolds stresses remain as unknowns. They should be determined separately and at this point turbulence models comes into the picture. In turbulence models Reynolds stresses can be modeled by turbulent-viscosity hypothesis, or more directly, by Reynolds-stress equations. In this study two different turbulence models, namely S-A and Menter's SST, which are among the turbulent-viscosity models, are used.

The mean momentum equation, according to the turbulent-viscosity hypothesis, be-

comes,

$$\frac{\bar{D}}{\bar{D}t}\bar{V} = \frac{\partial}{\partial x_i}\left[\nu_{eff}\left(\frac{\partial \bar{V}_i}{\partial x_j} + \frac{\partial \bar{V}_i}{\partial x_i}\right)\right] - \frac{1}{\rho}\frac{\partial}{\partial x_j}\left(\bar{p} + \frac{2}{3}\rho k\right) \tag{2.11}$$

where ν_{eff} is the effective viscosity and it is summation of molecular and turbulent viscosities, $\nu_{eff} = \nu + \nu_t$, $\frac{\bar{D}}{\bar{D}t}$ is mean substantial derivative, $\bar{V}_i$ and $\bar{V}_j$ are i and j components of mean velocity vector and $\frac{2}{3}\rho k$ is modified mean pressure. If ν_t can be specified, the closure problem is solved, i.e. equation 2.11 can be solved and turbulence models aim at solving this closure problem.

2.1.2.1 Spalart-Allmaras Turbulence Model

This model is a one-equation turbulence model, which was suggested by Spalart and Allmaras [63]. The transport equation implemented as S-A model in SU^2 is equation 9 which is in "Near wall region, finite Reynolds number" section of the original study of Spalart and Allmaras [63].

Eddy viscosity ν_t is computed as,

$$\nu_t = \tilde{\nu} f_{v1}, \quad f_{v1} = \frac{\chi^3}{\chi^3 + C_{v1}^3}, \quad \chi \equiv \frac{\tilde{\nu}}{\nu}, \quad \mu_t = \rho \nu_t \tag{2.12}$$

ν is molecular viscosity and $\tilde{\nu}$ obeys the transport equation,

$$\frac{D\tilde{\nu}}{Dt} = c_{b1}\tilde{S}\tilde{\nu} + \frac{1}{\sigma}[\nabla((\nu + \tilde{\nu})\nabla\tilde{\nu}) + c_{b2}(\nabla\tilde{\nu})^2] - \left[c_{w1} f_w\right]\left[\frac{\tilde{\nu}}{d}\right]^2 \tag{2.13}$$

where

$$\tilde{S} \equiv S + \frac{\tilde{\nu}}{\kappa^2 d^2} f_{v2}, \quad f_{v2} = 1 - \frac{\chi}{1 + \chi f_{v1}} \tag{2.14}$$

where S is the magnitude of vorticity and d is the distance to the closest wall. The

function f_w is,

$$f_w = g\left[\frac{1+c_{w3}^6}{g^6+c_{w3}^6}\right]^{1/6}, \quad g = r + c_{w2}\big(r^6 - r\big), \quad r \equiv \frac{\tilde{\nu}}{\tilde{S}\kappa^2 d^2} \tag{2.15}$$

The constants of above equations are,

$$\begin{aligned} &c_{b1} = 0.1355, \quad \sigma = 2/3, \quad c_{b2} = 0.622, \quad \kappa = 0.41 \\ &c_{w1} = \frac{c_{b1}}{\kappa} + \frac{1+c_{b2}}{\sigma} c_{w2} = 0.3, \quad c_{w3} = 2, \quad c_{v1} = 7.1 \end{aligned} \tag{2.16}$$

At the wall, boundary condition $\tilde{\nu} = 0$ is applied, while at far-field Spalart and Allmaras suggests a finite value for $\tilde{\nu}$ which is below $\nu/10$.

Equation 2.13 is implemented to the code as the convective, viscous and source terms as follows,

$$\vec{F}_c = \vec{v}\tilde{\nu}, \quad \vec{F}_v = \frac{\nu+\tilde{\nu}}{\sigma}\nabla\tilde{\nu}, \quad Q = c_{b1}\tilde{S}\tilde{\nu} - \Big[c_{w1}f_w\Big]\left[\frac{\tilde{\nu}}{d}\right]^2 + c_{b2}(\nabla\tilde{\nu})^2 \tag{2.17}$$

2.1.2.2 Shear-Stress Transport Turbulence Model

This is a two-equation turbulence-viscosity model, solving kinetic energy, k, and specific dissipation ω, which was suggested by Menter [47]. Menter suggested a model that is a blend of a $k-\omega$ formulation, which is based on Wilcox model [74] and standard $k-\epsilon$ model, and by blending them aimed improvement in performance over both $k-\omega$ and $k-\epsilon$ models.

Let ϕ_1 represent any constant in the original $k-\omega$ model, ϕ_2 represent the constants in $k-\epsilon$ model and F_1 be the blending function. Multiply the original $k-\omega$ model by the blending function, while multiplying $k-\epsilon$ model by $(1-F_1)$ and add them together,

$$\phi = F_1\phi_1 + (1-F_1)\phi_2 \tag{2.18}$$

so the two equations of new model becomes,

$$\frac{D\rho k}{Dt} = \tau_{ij}\frac{\partial v_i}{\partial x_j} - \beta^*\rho\omega k + \frac{\partial}{\partial x_j}\left[(\mu + \sigma_k\mu_t)\frac{\partial k}{\partial x_j}\right] \tag{2.19}$$

and

$$\frac{D\rho\omega}{Dt} = \frac{\gamma}{\nu_t}\tau_{ij}\frac{\partial v_i}{\partial x_j} - \beta\rho\omega^2 + \frac{\partial}{\partial x_j}\left[(\mu + \sigma_\omega\mu_t)\frac{\partial \omega}{\partial x_j}\right] + 2\rho(1-F_1)\sigma_{\omega 2}\frac{1}{\omega}\frac{\partial k}{\partial x_j}\frac{\partial \omega}{\partial x_j} \tag{2.20}$$

where the blending function F_1 is,

$$\begin{aligned} F_1 &= tanh(arg_1^4) \\ arg_1 &= min\left[max\left(\frac{\sqrt{k}}{0.09\omega y}; \frac{500\nu}{y^2\omega}\right); \frac{4\rho\sigma_{\omega 2}k}{CD_{k\omega}y^2}\right. \\ CD_{k\omega} &= max\left(2\rho\sigma_{\omega 2}\frac{1}{\omega}\frac{\partial k}{\partial x_j}\frac{\partial \omega}{\partial x_j}\right) \end{aligned} \tag{2.21}$$

where y is the distance to the next surface. The constants in equations 2.19, 2.20 and 2.21 are,

$$\begin{aligned} &\sigma_k = F_1\sigma_{k1} + (1-F_1)\sigma_{k2}, \quad \sigma_{k1} = 0.5, \quad \sigma_{k2} = 1.0 \\ &\sigma_\omega = F_1\sigma_{\omega 1} + (1-F_1)\sigma_{\omega 2}, \quad \sigma_{\omega 1} = 0.5, \quad \sigma_{\omega 2} = 0.856 \\ &\beta = F_1\beta_1 + (1-F_1)\beta_2, \quad \beta_1 = 0.0750, \quad \beta_2 = 0.0828 \\ &\gamma = F_1\gamma_1 + (1-F_1)\gamma_2, \quad \gamma_1 = \frac{\beta_1}{\beta^*} - \sigma_{\omega 1}\frac{\kappa^2}{\sqrt{\beta^*}}, \quad \gamma_2 = \frac{\beta_2}{\beta^*} - \sigma_{\omega 2}\frac{\kappa^2}{\sqrt{\beta^*}} \\ &\beta^* = 0.09, \quad \kappa = 0.41 \end{aligned} \tag{2.22}$$

The term arg_1 works as a switch case between $k-\omega$ and $k-\epsilon$ models. The arguments in arg_1 have finite values inside the boundary layer. However, they approaches to zero far enough away from the wall (near the boundary-layer edge) since all three terms have the wall distance value, y, as denominator. As arg_1 goes to zero, blending function F_1 goes to zero, too, and beyond that distance $k-\epsilon$ model is used.

There is another blending function, F_2 for turbulent viscosity term. Turbulent viscosity is calculated by,

$$\nu_t = \frac{a_1 k}{max(a_1\omega; \Omega F_2)}) \tag{2.23}$$

where $a_1 = 0.31$, Ω is the absolute value of vorticity and F_2 is,

$$\begin{aligned} F_2 &= tanh(arg_2^2) \\ arg_2 &= max\left(2\frac{\sqrt{k}}{0.09\omega y}; \frac{500\nu}{y^2\omega}\right) \end{aligned} \tag{2.24}$$

where F_2 is a function that has the value of one in boundary layer and zero for shear layer flows.

2.1.3 Non-dimensionalization of Governing Equations

Non-dimensional form of governing equations and boundary conditions are employed for flow solutions. The flow solver employed in this study has several alternatives to non-dimensionalization procedure; free-stream pressure value may be equated to one, free-stream velocity may be equated to one or free-stream velocity may be equated to Mach number. In this study non-dimensionalization is performed by equating the free-stream velocity value to Mach number. Based on White [70] and Palacios et al. [51], the non-dimensional parameters are,

$$\begin{aligned} &x^* = \frac{x}{L}, \quad y^* = \frac{y}{L}, \quad z^* = \frac{z}{L}, \quad t^* = \frac{tv}{L}, \quad \vec{v}^* = \frac{\vec{v}}{a} \equiv M \\ &p^* = \frac{p}{\gamma p_{ref}}, \quad \rho^* = \frac{\rho}{\rho_{ref}}, \quad T^* = \frac{T}{T_{ref}}, \quad \mu^* = \frac{\mu}{\mu_{ref}} \quad k^* = \frac{k}{k_{ref}} \end{aligned} \tag{2.25}$$

where the reference length is chord length, reference velocity magnitude, v_{ref}, is speed of sound, denoted by a, and the other reference values are given in table 2.1,

Table 2.1: Reference values used to non-dimensionalization of the problem [51]

Pressure	$p_{ref} = p_{\infty}$
Density	$\rho_{ref} = \rho_{\infty}$
Temperature	$T_{ref} = T_{\infty}$
Dynamic viscosity	$\mu_{ref} = \rho_{ref} v_{ref} L_{ref}$
Specific energy	$e_{ref} = {v_{ref}}^2$
Gas constant	$R_{ref} = e_{ref}/T_{ref}$
Specific heat at constant pressure	$C_{p_{ref}} = R_{ref}$
Heat conductivity	$k_{ref} = C_{p_{ref}} \mu_{ref}$
Stress	$\tau_{ref} = {v_{ref}}^2$
Turbulent specific dissipation	$\omega_{ref} = v_{ref}/L_{ref}$

2.1.4 Boundary Conditions

In this study, body forces are neglected, and the flow is assumed adiabatic. No-slip wall boundary condition is applied with zero heat flux. The flow field is assumed to be symmetric about the mid-span at $y = 0$, and symmetry boundary condition is applied at plane $y = 0$. The far-field boundary condition is applied at the far-field boundaries.

2.1.5 Solver Setup

In the current study, flow is described by steady-state Reynolds-averaged Navier-Stokes (RANS) equations, coupled with S-A and k-ω SST turbulence models. Convective fluxes are evaluated by a second order accurate scheme, JST (Jameson-Schmidt-Turkel), and Weighted Least Squares methods are employed to gradient calculations of flow variables. Although the flow field is represented by steady-state equations, the system is still needed to be discretized in time domain. Implicit Euler scheme is employed for temporal discretization in the study. In addition, local-time stepping technique is used by SU^2 in order to accelerate the convergence [51]. To solve the implicit problem Flexible Generalized Minimal Residual (FGMRES) method is used with Incomplete Lower Upper (ILU) factorization.

2.2 Computational Grid Generation

It is known that, for boundary layer flows, velocity gradient is much higher along the surface normal than the velocity gradient along flow direction. Therefore, discretizing the boundary layer region by the cells having small sizes along surface normal but stretched along the flow direction is an appropriate technique. On the other hand, outside of the boundary layer, there is no need to those kind of stretched cells. In this study, too, a similar meshing strategy is used, a hybrid grid configuration is employed to the computational domain. The 3D computational domain is discretized by stretched prismatic cells in boundary layer, while tetrahedral cells are employed at the outside of boundary layer region. Pyramidical cells are also used if they are required during transition from prismatic to tetrahedral cells. In turbulent flow solutions, first cell thickness of prismatic boundary layer mesh is determined by such a way that y^+ value is kept around one. No wall function is applied in this study, thus, $y^+ \approx 1$ reveals as a requirement of the employed turbulence models. Prismatic cells' growth ratio along the surface normal is kept as 1.2 and prismatic cell region reaches up to boundary layer is completely covered.

2.2.1 Solution Adaptive Grid Refinement

The mesh convergence strategy in this study is using solution adaptive mesh refinement technique. This methodology is available in SU^2 and based on an anisotropic grid refinement process suggested by Biswas and Strawn [6, 5]. This method uses two criteria; an error indicator and allowed number of new grid nodes which can be created in each adaptation level. The error indicator shows the tetrahedral cells having density gradients above the software defined threshold value. These cells are flagged for cell division, or the refinement process. The software defined threshold starts from the normalized value of 1 and is lowered until the number-of-new-nodes criteria is exceeded. This node-number criteria is a user-defined value which determines the ratio of allowed number of new nodes that can be created to the old ones. During the subdivision process, buffer cells are created around the flagged cell faces and subdivision is carried out without generating any hanging nodes. This refinement technique is only be applied to tetrahedral cells, while 2D boundary cells and prismatic boundary

layer cells are not altered.

2.3 Optimization Framework

One of the aims of this study is improving aerodynamic performance of a close-coupled delta wing-canard configuration by performing a configuration parameters optimization. Although employed flow field solver SU^2 has a built-in and entirely automated gradient-based optimization tool, it was not applicable to configuration optimization because of the fact that such large deformations needed by configuration optimization process could not handled by SU^2 shape optimization suite. Therefore this study also aimed at constructing an optimization cycle that utilizes fluid flow calculations, sensitivity and gradient evaluations, optimization algorithms and mesh deformation processes, in a fully automated manner, in order to optimize the configuration and the flowchart can be seen in figure 2.1.

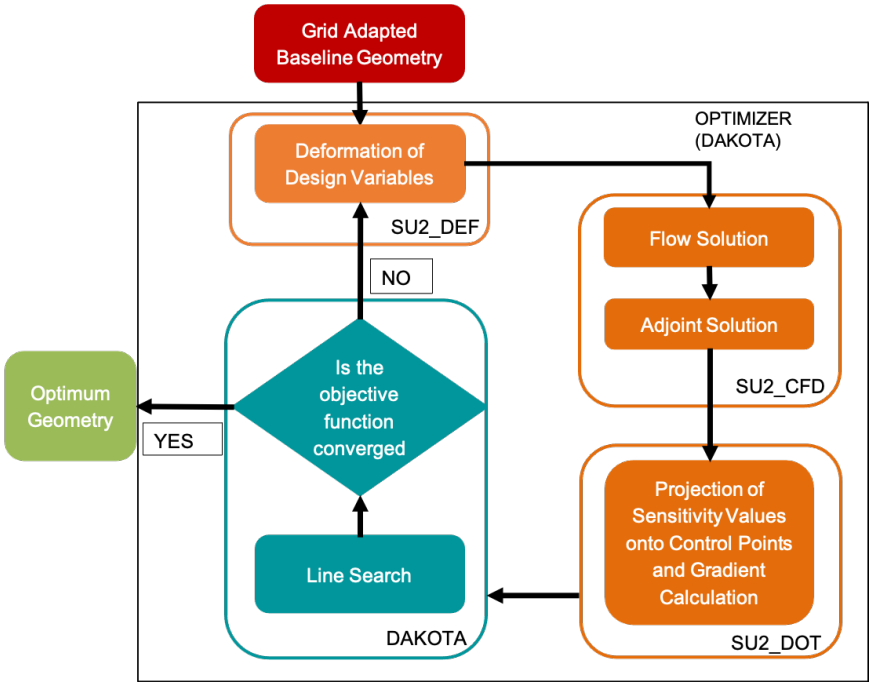

Figure 2.1: Optimization cycle flowchart

The optimization process is applied to a close-coupled delta wing-canard configuration. The process begins with a grid-adapted mesh of the baseline design, which is a generic delta wing-canard configuration in this study. The entire optimization

process is controlled by the DAKOTA software. First, initial deformation conditions are applied to the geometry, via the control points on FFD box, and computational grid is deformed by the mesh deformation tool `SU2_DEF`. Then, flow field and adjoint based sensitivities are evaluated by `SU2_CFD` module. Then, sensitivity values are projected onto the control points of FFD box by `SU2_DOT` module and gradients are evaluated. Optimization algorithm is included in DAKOTA. DAKOTA software communicates with SU^2, to get the gradients, approximates the Hessian, itself and searches the optimum values of design variables in the design step. At the last step of the cycle, convergence criteria is checked and if the criteria is not satisfied the new deformations are applied to design variables for the new design step. The cycle is repeated until the convergence criteria, or the local minimum point, is satisfied.

2.4 Gradient-Based Optimization

Gradient-based methods require to find the direction which drives the objective function to its minimum (or maximum). This direction is the gradient, or sensitivity derivatives of objective function with respect to design variables. Once the sensitivity analysis is done, optimization algorithm evaluates the amounts of changes in design variables to achieve the minimum point. In the present study, DAKOTA software is employed into to the study which includes the quasi-Newton method as optimization algorithm. The quasi-Newton method class which is implemented in the DAKOTA is based on the Meza's study [48]. Optimization cycle is terminated if local minimum point is reached. In order to verify that local minimum is reached, the Hessian, $H = \nabla^2 f$, should be positive-definite. Hence, calculation of Hessian is also an essential step in the cycle. In this study Broyden-Fletcher-Goldfarb-Shanno (BFGS) method is employed to approximate the Hessian numerically. Here, the quasi-Newton algorithm uses the gradients provided by SU^2, and a gradient-based line search, which is based on the algorithm given by More and Thuente [49] is employed.

A general formulation of a constrained optimization problem is

$$\begin{aligned} \text{minimize :} \quad & f(\vec{x}), \quad \text{with respect to} \quad \vec{x} \in \mathbb{R}^n \\ \text{subject to :} \quad & g_L \leq g(\vec{x}) \leq g_U \\ & h(\vec{x}) = h_t \\ & a_L \leq A_i \vec{x} \leq a_U \\ & A_e \vec{x} = a_t \\ & \vec{x}_L \leq \vec{x} \leq \vec{x}_U \end{aligned} \tag{2.26}$$

where f is the objective function subjected to minimization, $\vec{x}$ is the vector of design variables with dimension of n, number of design variables, g and h are nonlinear inequality and equality constraints, respectively, while A_i and A_e are linear inequality and equality constraints and $\vec{x}_L$ and $\vec{x}_U$ are the geometric bounds of the problem.

For constrained problems a large variety of optimization algorithms are available, namely non-linear programming (NLP) methods, sequential quadratic programming (SQP) methods, Newton methods and etc. Quasi-Newton method is employed in this study which is in form of,

$$f(x_k + \Delta x) \approx f(x_k) + \Delta f(x_k)^T \Delta x \ + \frac{1}{2} \Delta x^T B \Delta x \tag{2.27}$$

where Δf is the gradient of f, and B is the approximation of Hessian.

2.4.1 Adjoint Based Sensitivity Calculations

The adjoint method suggests introducing an adjoint equation to the cost function in order to decouple the effect of design variables and flow variables to the objective function. It is achieved by solving an adjoint equation which has coefficients defined by the solution of flow equations and determining the gradients indirectly by this adjoint equation. This provides reducing the computational cost of gradient calculations approximately to the level of two flow solution cost, as independent of number of design variables. Klein [37] gives a comparison of computational costs of conven-

tional finite difference method and adjoint method for gradient calculations, in terms of number of design variables in figure 2.2.

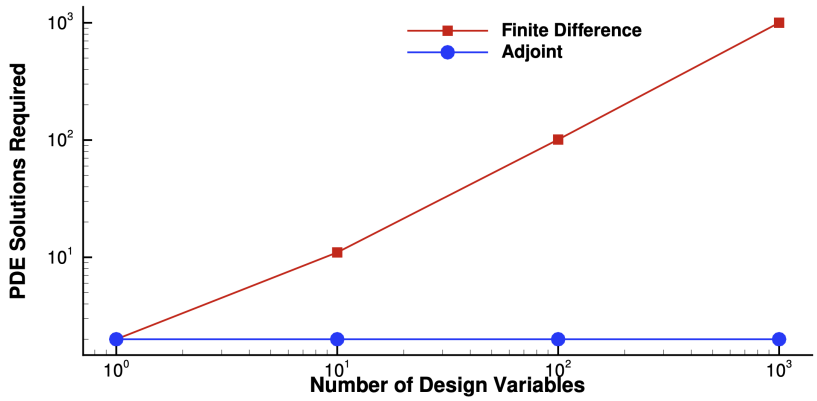

Figure 2.2: Number of PDE solutions required for gradient calculations vs. number of design variables, [37]

Adjoint methods are divided into two different discretization techniques, continuous and discrete. Mainly, both techniques offer discrete adjoint equations for state PDEs. In this study discrete adjoint approach is employed. Below, the general formulation and discrete approach of adjoint method is given in detail.

2.4.1.1 General Formulation of Adjoint Method

First, introduce an objective function, J, which is function of flow variables, U, and the design variables, x,

$$J = J(U, x) \tag{2.28}$$

Minimization of objective, or cost, function, can be provided by changing design variables, x. Therefore variation of J with respect to x should be calculated. However, since any variation in physical boundary of aerodynamic shape, which is related to design variables, also cause variations in state variables, variation in J due variation

in x becomes,

$$\delta J = \frac{\partial J^T}{\partial U}\delta U + \frac{\partial J^T}{\partial x}\delta x \tag{2.29}$$

Above equation shows that any changes in design variables also brings the necessity of reevaluation of flow field along, to evaluate the gradients. Control theory, or adjoint formulation, suggests introducing the flow field governing equations as constraint to optimization problem, so that gradient calculations does not require reevaluation of the flow field. So, δU should be eliminated from equation 2.29. Let R is the governing equation, function of flow variables, U, and the design variables, x,

$$R = R(U, x) = 0 \tag{2.30}$$

and

$$\delta R = \frac{\partial R}{\partial U}\delta U + \frac{\partial R}{\partial x}\delta x = 0 \tag{2.31}$$

Now, introduce a Lagrange multiplier, ψ which satisfies the following adjoint equation,

$$\left(\frac{\partial R}{\partial U}\right)^T \psi = \frac{\partial J}{\partial U} \quad \rightarrow \quad \frac{\partial J}{\partial U} - \left(\frac{\partial R}{\partial U}\right)^T \psi = 0 \tag{2.32}$$

Multiply equation 2.31 by ψ and substitute into 2.29. Since δR is set to zero, substitution does not violate the objective function. Now the objective function becomes,

$$\delta J = \delta J - \psi\delta R = \left(\frac{\partial J^T}{\partial U} - \psi^T\frac{\partial R}{\partial U}\right)\delta U + \left(\frac{\partial J^T}{\partial x} - \psi^T\frac{\partial R}{\partial x}\right)\delta x \tag{2.33}$$

Thus, by considering equation 2.32, objective function reduces to,

$$\delta J = \left(\frac{\partial J^T}{\partial x} - \psi^T\frac{\partial R}{\partial x}\right)\delta x \tag{2.34}$$

So, objective function becomes independent of flow variables, and solving only two equations, one adjoint equation (2.32) and one objective function (2.34) is enough for gradient calculations, regardless of the number of design variables.

As stated previously, this method has two approaches, continuous and discrete formulation. Below, mathematical expressions for discrete adjoint approach, which is used in this study, is given.

2.4.1.2 Discrete Adjoint Approach

In this methodology, the sensitivity of objective function with respect to design variables becomes,

$$\frac{dJ}{dx} = \frac{\partial J}{\partial U}\frac{dU}{dx} + \frac{\partial J}{\partial x} \tag{2.35}$$

and similarly sensitivity of governing equation is

$$\frac{dR}{dx} = \frac{\partial R}{\partial U}\frac{dU}{dx} + \frac{\partial R}{\partial x} = 0 \tag{2.36}$$

or,

$$\frac{dU}{dx} = -\left(\frac{\partial R}{\partial U}\right)^{-1}\frac{\partial R}{\partial x} \tag{2.37}$$

substitute equation 2.37 into objective function,

$$\frac{dJ}{dx} = -\frac{\partial J}{\partial U}\left(\frac{\partial R}{\partial U}\right)^{-1}\frac{\partial R}{\partial x} + \frac{\partial J}{\partial x} \tag{2.38}$$

Define a Lagrange multiplier, ψ, which satisfies the following adjoint equation,

$$\left(\frac{\partial R}{\partial U}\right)^{T}\psi = -\left(\frac{\partial J}{\partial U}\right)^{T} \tag{2.39}$$

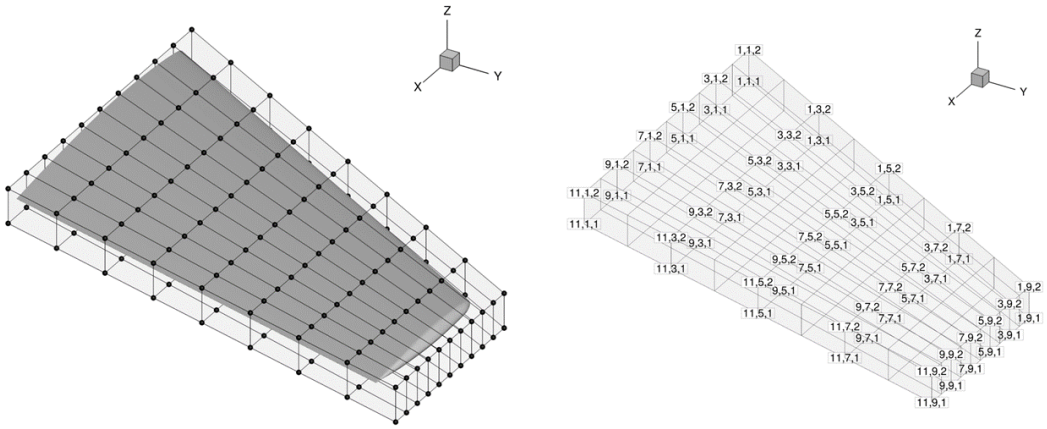

Figure 2.3: An example FFD box enclosing a wing, its control points and their indices

Then, sensitivity equation of objective function becomes

$$\frac{dJ}{dx} = \psi^T \frac{\partial R}{\partial x} + \frac{\partial J}{\partial x} \tag{2.40}$$

2.4.2 Surface Parametrization

In optimization problems, shape deformations are controlled by design variables. In this study, the baseline design is parametrized by an FFD box which encloses the canard geometry and control points, controlling the shape deformation, are assigned as design variables. An FFD box is a hexahedral box which is meshed in a lattice structure (figure 2.3). Each mesh node can be defined as control point and can freely move in all three directions.

In this study, the control points of FFD box are the eight vertex points of this box. Two degrees of freedom are assigned to the control points, translations along x and z directions. Projections of sensitivity values on those points give the gradient of each control point. The FFD box is moved as a rigid block by the amount of averaged-gradient of those vertex points, since only the canard position is investigated.

2.4.3 Objective Function and Design Variables

The aim of the study is increasing the lift generated by a close-coupled delta wing-canard configuration at specific design conditions requires that C_L value to be as high as possible. Therefore, C_L is assigned as objective function and optimization process is employed to maximize this coefficient.

There are numerous possible design variables subjected to design optimization problem, such as span length, sweep angle, surface shape, wing or canard position etc. The configuration optimization is carried out in this study by changing the relative canard position, in other words moving the canard relative to wing, in body x and z directions. This translation of canard is provided by moving all eight vertex points of FFD box in two directions. Therefore 16 design variables are determined in this study. The literature review show that canard lift increment is almost independent from canard deflection angle, however it can be significantly improved by horizontal and vertical positioning of the canard. On the other hand, C_M strongly depends on canard deflection angle and also its horizontal distance from the neutral point. Since the objective function is maximization of C_L and there is no constraint, such as C_D or C_M, other than geometric bounds, it is concluded that horizontal and vertical translations of canard are sufficient design variables for this study.

CHAPTER 3

RESULTS AND DISCUSSION

In this chapter, first, the flow solver SU^2 is verified on solution adaptive grids for such vortical flows by referencing two experimental studies conducted in Technical University of Braunschweig [4, 50]. The flow field is investigated extensively as well as verification cases are evaluated. The adjoint-based configuration optimization cases are performed on the geometry given in figure 3.1b at 8.7° and 20° angles of attack on viscous flows. The results are presented and discussed in detail.

3.1 Reference Study

In Technical University of Braunschweig, Hummel et al. conducted a series of experiments on close-coupled delta canard-wing configurations. Their studies and observations are widely used in literature as benchmarking and reference cases. Since there are both several experimental and numerical data is available in literature, those two generic models [50, 4] are taken as reference, or baseline geometries. Both geometries have canard and wing planforms of 2.31 aspect ratio and 60° leading-edge sweep angles. Wing and canard airfoils are symmetric circular arc airfoils with 1-mm-thick leading- and trailing-edges. This thickness is regarded as sharp-edge by authors, Bergmann et al. The experiments are conducted at Mach number of 0.177 and $Re = 1.4 \times 10^6$. Available flow field data are at $\alpha = 8.7^\circ$ for the case of [50] and at $\alpha = 20^\circ$ and $\alpha = 30^\circ$ for [4]. Oil flow visualization of surface streamlines, spanwise surface pressure distributions and total pressure coefficient contours at several section on wing are the available flow field data and integrated lift, drag and moment coefficient curves are also provided.

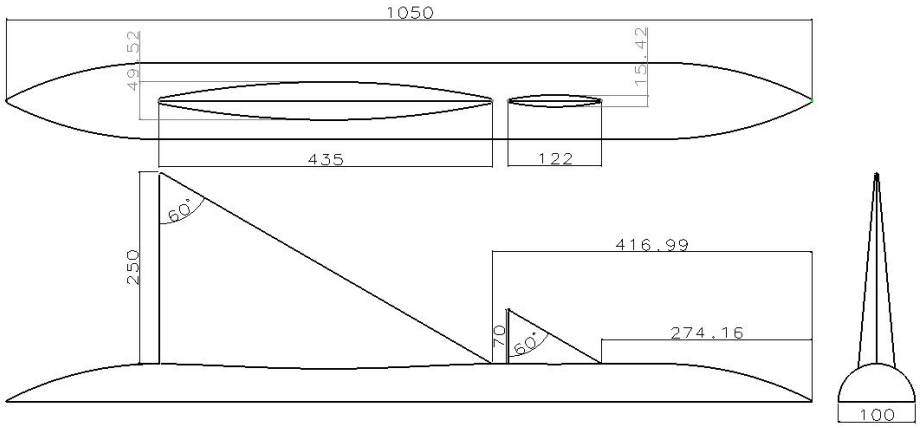

(a) Canard-wing configuration of reference study [4]

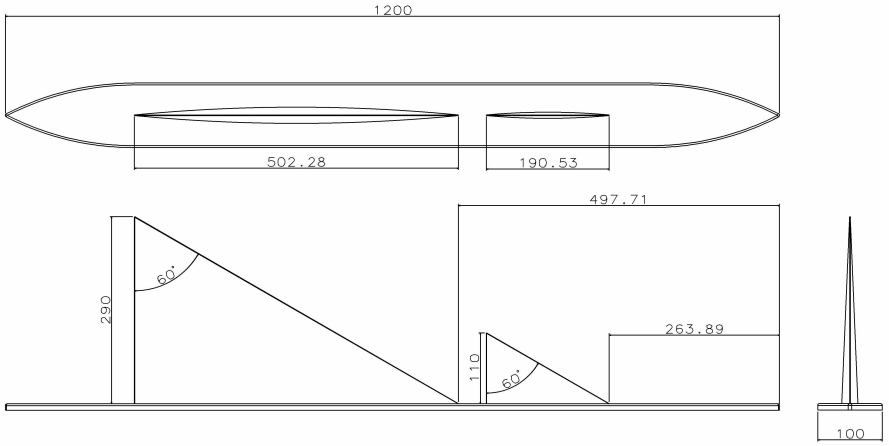

(b) Canard-wing configuration of reference study [50]

Figure 3.1: Reference geometries employed in the study and their dimensions

In this study, three angles of attack cases, $\alpha = 8.7°$, $20°$ and $30°$, are considered for verification purposes and two angle of attack cases, $\alpha = 8.7°$ and $20°$, for optimization purposes.

The grid independent solutions are obtained by varying the boundary layer grid resolution by hand and employing the solution adaptive grid refinement technique for the rest of tetrahedral volume cells.

3.2 Parallel Performance of SU^2

Computations are performed in the parallel computing environment of METUWIND HPC lab. The HPC cluster consists of 8 computer nodes each of which has 4 AMD Opteron 6276 2.30 GHz CPUs with 16 cores. Those nodes are connected to a 10 GHz Ethernet and forms a total of 512-core computer. The parallel computation performance of the SU^2 solver for the current problem is given by a speed-up plot in figure 3.2. The calculation speed increases close to ideal speed-up line up to 16 cores, belonging to a single CPU and slightly deviates from ideal line up to 64 cores which are belong to a single node. Employing a further number of cores to the problem decreases the parallel efficiency rapidly since massage passing between the nodes now results a significant time consumption. Therefore, 64 cores within a single node are employed to the flow and adjoint calculations.

By using 64 cores, the flow and adjoint solutions take about 13 and 9:15 hours wall time, or 832 and 592 CPU hours, for a grid of 13-million cells, respectively. As the result, in optimization problem, completing one design cycle takes about 1500 CPU hours.

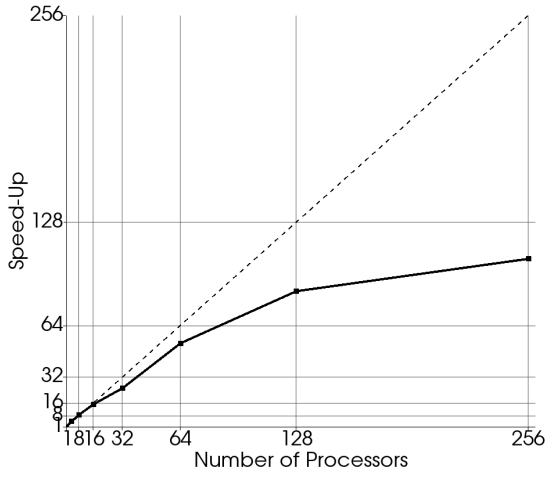

Figure 3.2: Speed-up of SU^2 solutions

3.3 Verification of SU^2

Fully turbulent viscous, RANS, flow solutions are compared to measurements in order to verify the flow solver and numerical methods. Prior to flow field and optimization studies, adapted grids and turbulence models are assessed based on the pressure distribution comparisons between numerical predictions and experimental measurements. Vortical flow fields over the geometry are investigated in detail, optimization studies are employed and evaluation of flow field on optimized geometries are studied after the verification of solver is assessed. The verification of numerical methods is evaluated at 30° angle of attack since the effects of grid adapted grids and success of turbulence models on prediction of breakdown can be clearly seen on pressure distributions at this angle and experimental data are available.

3.3.1 Computational Grid

The grid generation process starts with generating 2D surface cells. A relatively fine mesh resolution is employed all over the geometry, while leading and trailing edges are meshed in a much higher cell density in order to accurately resolve leading edge curvature and leading-edge flow separations (see figure 3.3).

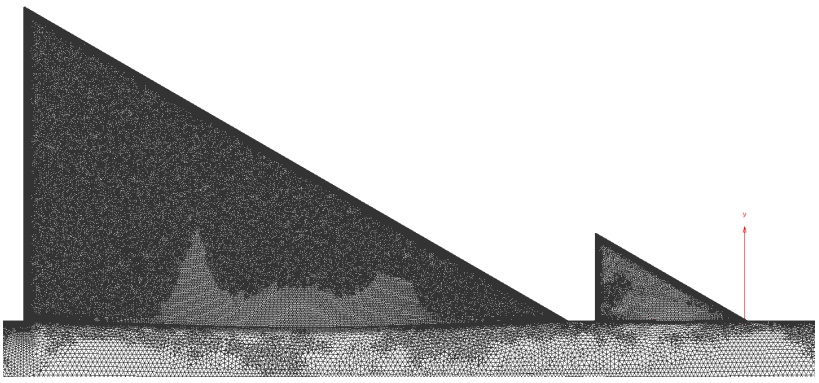

Figure 3.3: 2D surface grid resolutions on the geometry

For viscous flow solutions, triangular surface cells are extruded along the surface normals to create prismatic boundary layer cells. As stated in chapter 2.2, boundary layer grid is created in such a way that first layer thickness above the surface has dimensionless value of $y^+ \approx 1$ due to the turbulence modeling requirement and grow with the

ratio of 1.2 until boundary layer is fully resolved by prismatic cells. A sufficient y^+ distribution over the geometry is reached, as seen in figure 3.4, y^+ values are mostly around 1-1.5. The grid refinement technique which is employed to tetrahedral cells does not handle prismatic cells and therefore prismatic cell resolution is well studied. The rest of computational volume is meshed by tetrahedral cells. Volume cells are given in figures 3.5 and 3.6.

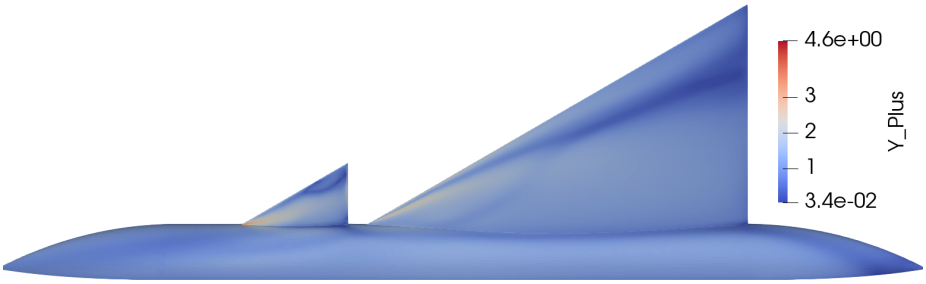

Figure 3.4: y$^+$ distribution on the upper surface, $\alpha = 30°$

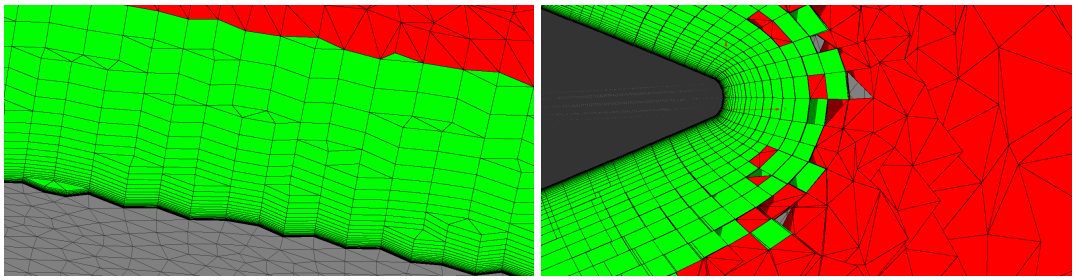

Figure 3.5: Prismatic boundary layer cells

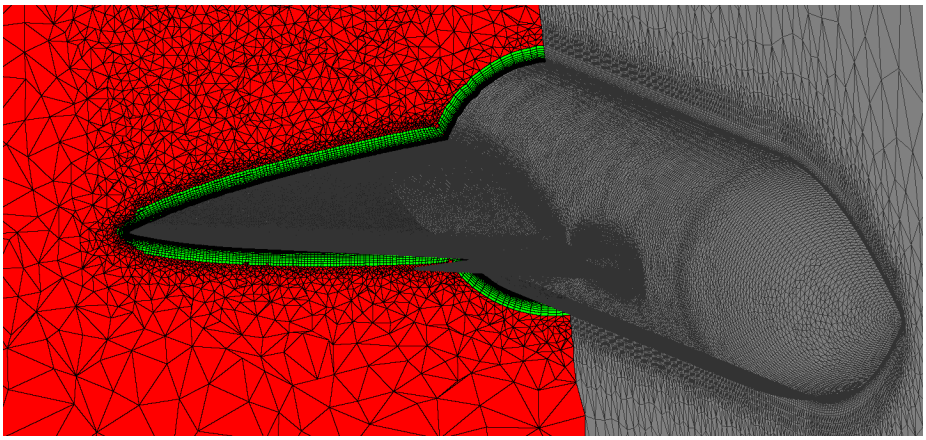

Figure 3.6: Hybrid volume grid over the geometry, at wing section $x/c = 0.65$

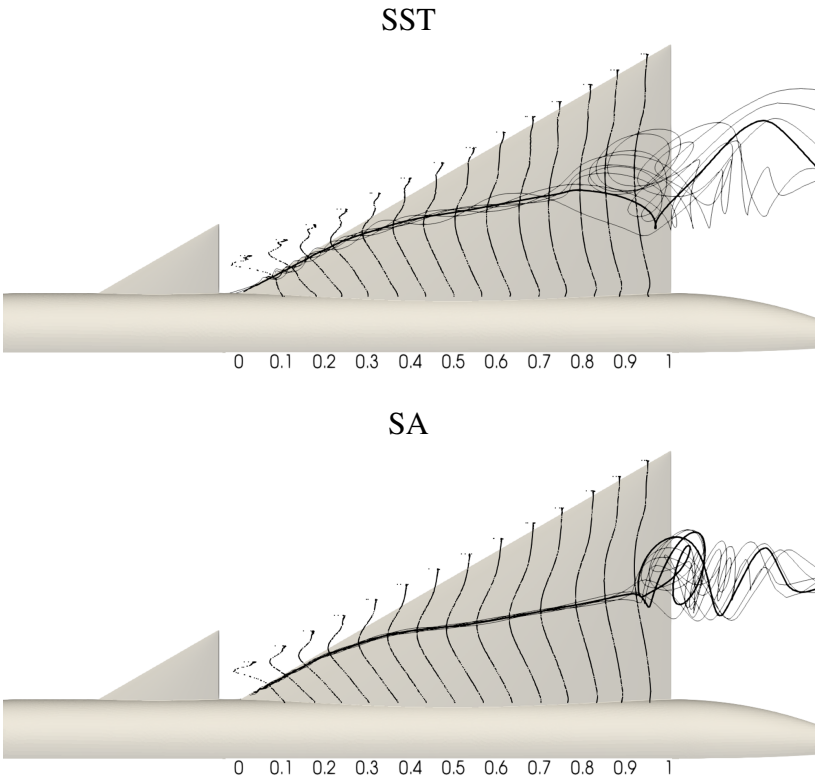

Figure 3.7: Surface pressure distributions and vortex core streamlines of turbulence models, $\alpha = 30°$

3.3.2 Assessment of Turbulence Models

The turbulent flow fields are represented by S-A and Menter's $k - \omega$ SST models at $\alpha = 30°$. The employed computational hybrid grid which is also shown in figure 3.6 consists of 7.8 million prismatic boundary layer cells above the model surface with first layer thickness of $y^+ \approx 1$ and 10.5 million volume cells in total. Turbulence models are assessed before grid adaptation is employed, so this grid will be named as "baseline" grid in next grid refinement section.

In figure 3.7 the span-wise trajectory of wing vortex is shown by streamlines passing through the vortex core and span-wise pressure distributions along the wing are plotted. The strong leading-edge separation forms a stable vortex sheet in which the fluid flows with high axial velocity. This axial velocity makes streamlines at the vortex core flow along a straight axial path. On the other hand, breakdown of this stable vortex can be identified by sudden burst of vortex core that causes dramatic changes

on jet-like axial flow at core. Therefore vortex breakdown can be visualize by tracking the streamlines passing through the vortex core. As shown in figure 3.7, both turbulence models predict similar vortex trajectories ahead of the breakdown. On the other hand, breakdown is predicted at quite different locations by those two turbulence models, the SST models predicts the vortex breakdown at about 80% of wing root chord, while it is predicted at $x/c > 90\%$ in the case of S-A model.

In figures 3.8 and 3.9 differences on vortex strength predictions of two turbulence models are clearly seen. The computed pressure distributions are compared to the experimental data [4]. Previous studies on the mechanism of vortex breakdown show that a strong deceleration of axial velocity and corresponding decrease of suction pressure occurs just before the vortex bursting. In figure 3.9, decrease in magnitude of negative C_p is seen between $40\% - 64\%$ of the wing root chord, due to experimental measurements. SST model accurately predicts this decrease, while S-A model is still predicting that vortex preserves most of its strength at $x/c = 0.64$.

It is known in literature that, S-A turbulence model is not successful in such free shear layer flows. Also considering the numerical results discussed above, it is concluded that the SST turbulence model provides better estimations of turbulent flow fields and strengths of suction regions and breakdown location are in a better agreement with measurements. Therefore, the SST model is employed in viscous simulations in the remaining of the study.

3.3.3 Solution Adaptive Grid Refinement

In order to capture the vortex dynamics, including breakdown, accurately and reach grid-independent solutions, solution-based grid refinement methodology, available in SU^2 is employed. The tetrahedral cells of baseline grid is refined based on solution density gradients in three levels. At each adaptation level, the total number of grid nodes are allowed to increase by 20%, as given in table 3.1

For each angle attack case, adaptive grid refinement applied, separately. Here, $\alpha = 30^\circ$ is given as example case. The vorticity contours are shown in figure 3.10, with volume grids. As observed, beginning from the first adaptation level, refined grid cells

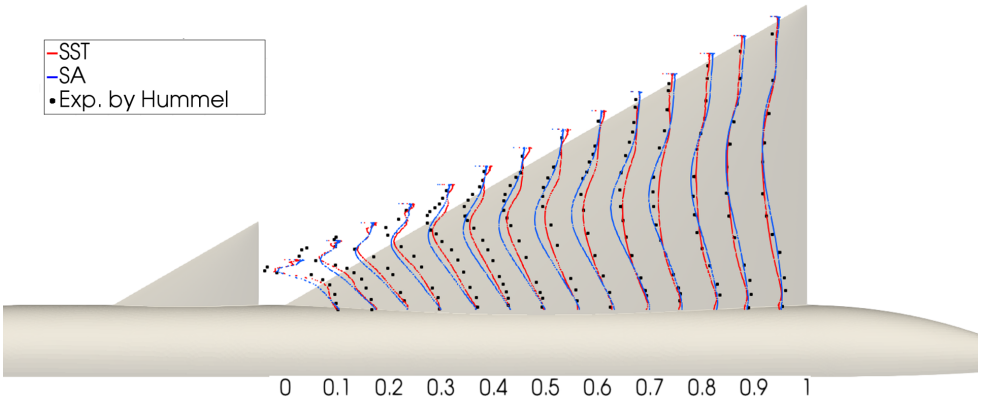

Figure 3.8: Surface pressure distributions of two turbulence models and experiment [4] over the wing, $\alpha = 30°$

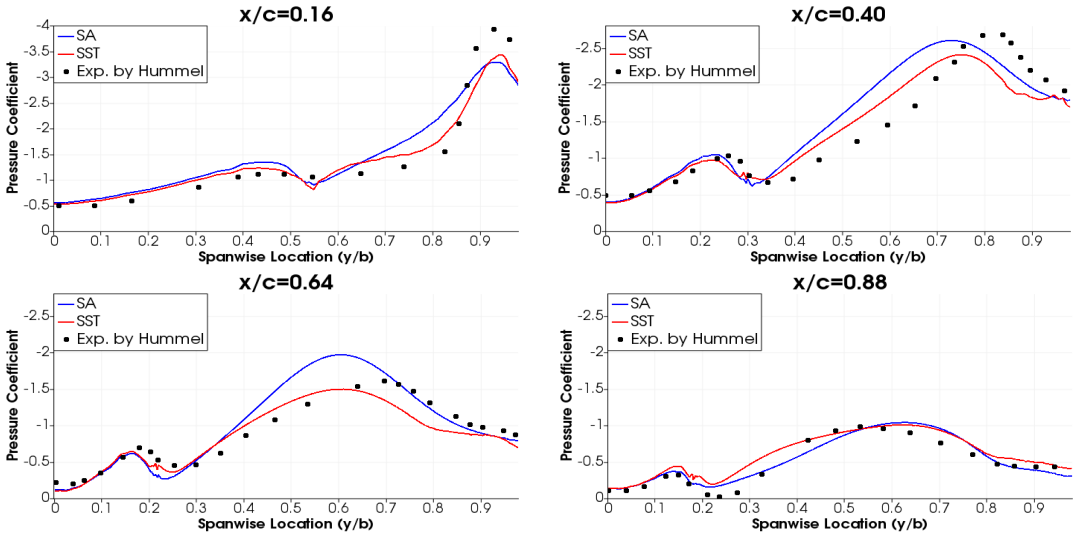

Figure 3.9: Surface pressure distribution of two turbulence models and experiment [4], $\alpha = 30°$

are clustered around the canard and wing vortices. As the vortex region cells refined, vortex structures are captured sharper, in other words, diffusions in vorticity field due to cell resolution is reduced. Therefore, larger vorticity magnitudes are observed in vortex region. At the third level, it is seen that vortex region is not refined intensively anymore, but also volume cells at wake region and cells away from vortex regions are started to be refined.

In figures 3.11 and 3.12, variations in span-wise C_p distributions, due to grid re-

Table 3.1: Number of cells in solution adaptive grid refinement levels, $\alpha = 30^{\circ}$ case

	Tetrahedral Cells	Total Cells
Baseline Grid	$2.605 \cdot 10^6$	$10.563 \cdot 10^6$
Adaptation Level 1	$5.058 \cdot 10^6$	$12.999 \cdot 10^6$
Adaptation Level 2	$8.341 \cdot 10^6$	$16.275 \cdot 10^6$
Adaptation Level 3	$12.918 \cdot 10^6$	$21.025 \cdot 10^6$

finement is given. In figure 3.11, it is observed that a significant improvement in suction pressures is achieved by first refinement process, while the second and third refinement steps do not as much as first step. One can see the improvements in numerical predictions achieved by grid adaptation technique in figure 3.12. The predicted pressure distribution is in a very well agreement with the experimental measurements throughout the wing. Suction peaks, indicating canard and wing vortices, minimum pressure values and vortex bursting are accurately predicted by the numerical setup employing RANS equations coupled with SST turbulence model, and one-level adapted grid. Then, flow solution provided by one level of grid adaptation is considered as grid independent.

3.4 Evaluation of Flow Field over a Canard-Wing Configuration

3.4.1 Canard-Wing configuration at $\alpha = 8.7^{\circ}$

The canard-wing configuration is first studied for a low-angle-of-attack case. The configuration is subjected to a flow angle of $\alpha = 8.7^{\circ}$, where the surface oil flow and cross-sectional total pressure coefficient contours are also available [50]. The numerical results are obtained by employing the SST turbulence model and one level solution-adapted grid, as extensively discussed in previous sections. The results are obtained from a solution which satisfies a five-order reduction in root-mean-square of density residual in log10 form. Residual and aerodynamic coefficient convergence histories are seen in figure 3.13.

The surface streamline view in figure 3.14 presents a qualitative comparison to flow

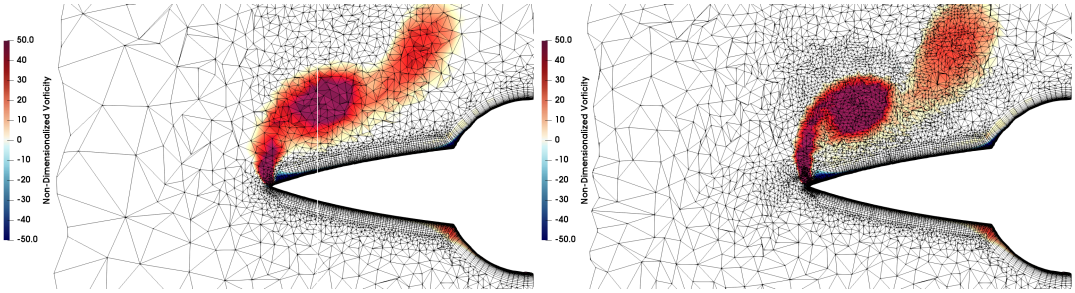

Baseline Grid

Refinement Level 1

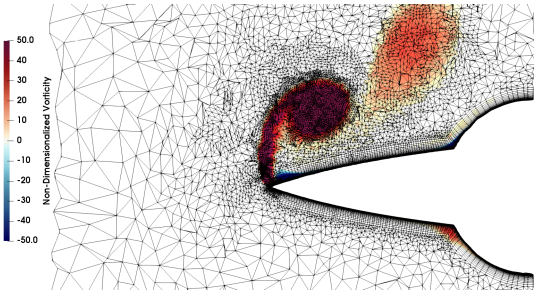

Refinement Level 2

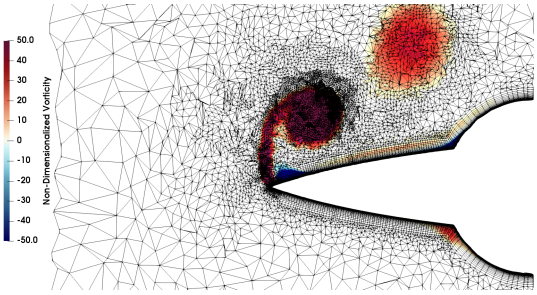

Refinement Level 3

Figure 3.10: Vorticity contours and mesh resolutions at wing section $x/c = 0.40$, $\alpha = 30°$

captured in the experiment with oil flow visualization. Numerical solution reveals a good agreement with experimental observations in terms of reattachment lines which are also draw the borders of canard and wing primary vortices. In addition, numerical calculations are also good at capturing the secondary vortex on wing, which exists in between the primary vortex and wing leading edge.

Both surface streamlines and oil flow visualization in figure 3.14 clearly shows that leading-edge separation region starts at fairly further downstream of wing apex, which results from the well-known downwash effect of canard on the inboard section of wing. On the other hand, at downstream, close to the wing trailing edge, wing vortex reaches size and location of suction peak of canard-off case (figure 4c of ref. [50]), although the wing works in a less effective angle of attack because the canard downwash. This recovery in suction force at the rear sections of wing is due to the upwash effect of the canard affecting the outboard sections of wing. However, the wing vortex trajectory in this case moves much closer to the wing leading edge with respect to other high-angle-of-attack cases examined in this study, one of which can be seen

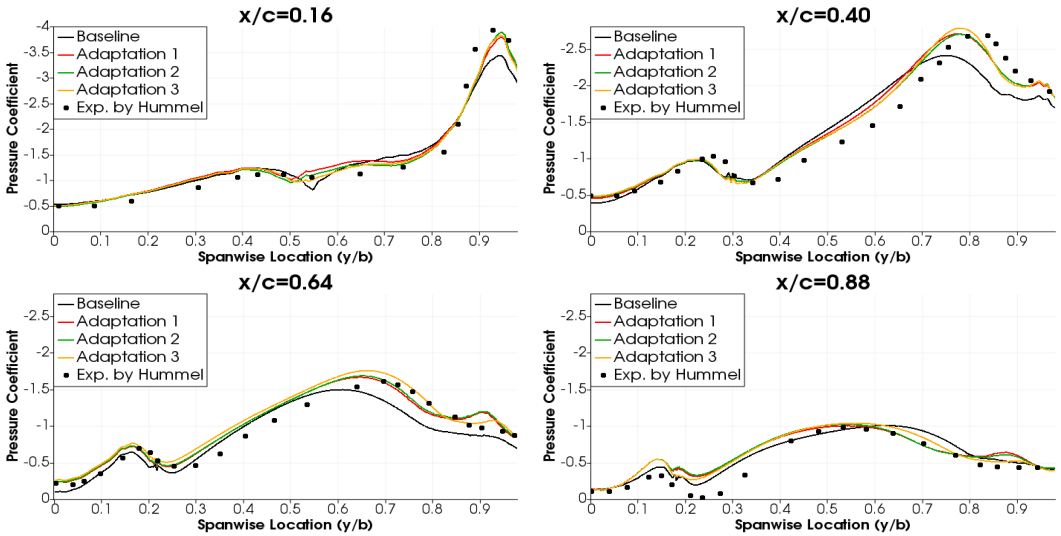

Figure 3.11: Surface pressure distributions of grid adaptation levels and experiment [4], $\alpha = 30°$

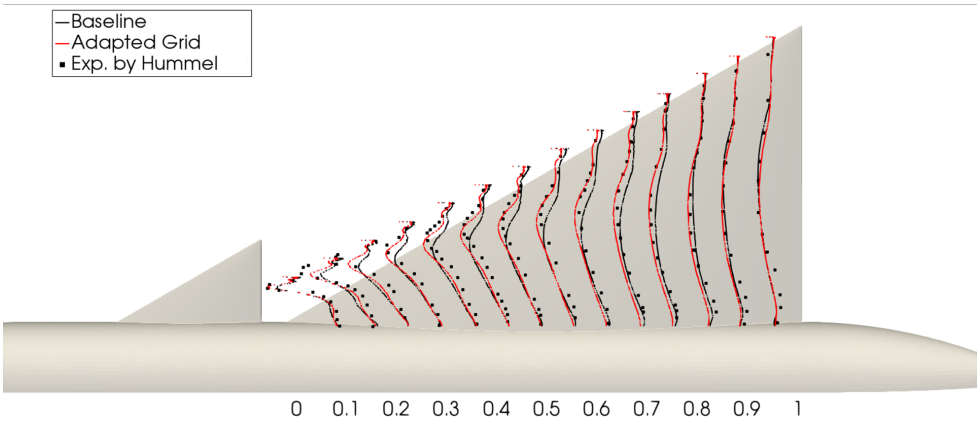

Figure 3.12: Surface pressure distributions of base and one-level-adapted grids and experiment [4], $\alpha = 30°$

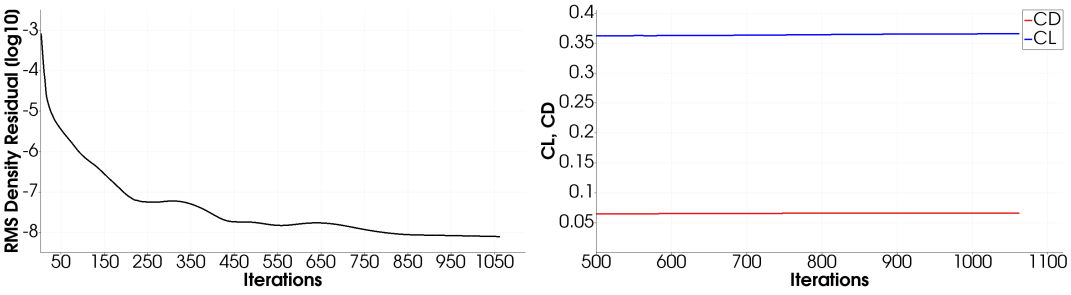

Figure 3.13: Convergence history of flow solution, $\alpha = 8.7°$

in figure 3.22. The fact that vortex trajectory does not move towards the inboard of wing, reveals that the influence of canard vortex at this angle is not that much strong.

Figure 3.15 presents both qualitative and quantitative evaluation of 3D flow structure over the configuration at this angle of attack. First of all, the comparison of numerical solutions and experimental measurements are given together for verification purposes. As seen, calculations reveal a good agreement with measurements at every cross-plane sections.

At the uppermost figure of figure 3.15 which is at wing apex ($x/c = 0.0$), there are two counter-rotating vortices which are partly separated by a throat. One of these vortices is canard's leading-edge separation vortex and the other one is trailing edge vortex. These vortices have distinct centers at approximately 95% and 80% of canard span length, relatively. At the middle figure, total pressure loss on a plane cut at 30% of wing chord is shown. Here, canard vortex system is seen as a merged vortex having only one vortex core. On the wing surface, the formation of wing leading-edge separation vortex can be seen. At this location, it is seen that pressure contours indicating the pressure loss due to wing boundary layer start merging with canard vortex system. This is because of that the canard vortex system moves downward towards the wing surface and "touch" the wing upper surface for $x/c < 0.60$ [50]. At the last figure of 3.15, calculations slightly differ from measurements. The current study predicts separated pressure loss iso-curves that identify canard vortex and wing boundary layer, while measurements show that canard vortex is still in touch with wing boundary layer. On the other hand, wing's primary and secondary vortices are predicted in a good accuracy, of which core is located approximately at 87% of wing span.

3.4.2 Canard-Wing configuration at $\alpha = 20^\circ$

It is known that the effect of canard is much more significant at higher angles of attack. Previous studies show vortex breakdown exists at $\alpha = 10^\circ$ on an isolated delta wing, while for a canard-wing configuration, it is improved to $\alpha \approx 20^\circ$. Therefore, investigating the vortex dynamics at such angles makes the effect of canard more definite. To unveil this effect, canard-off and canard-on configurations are considered

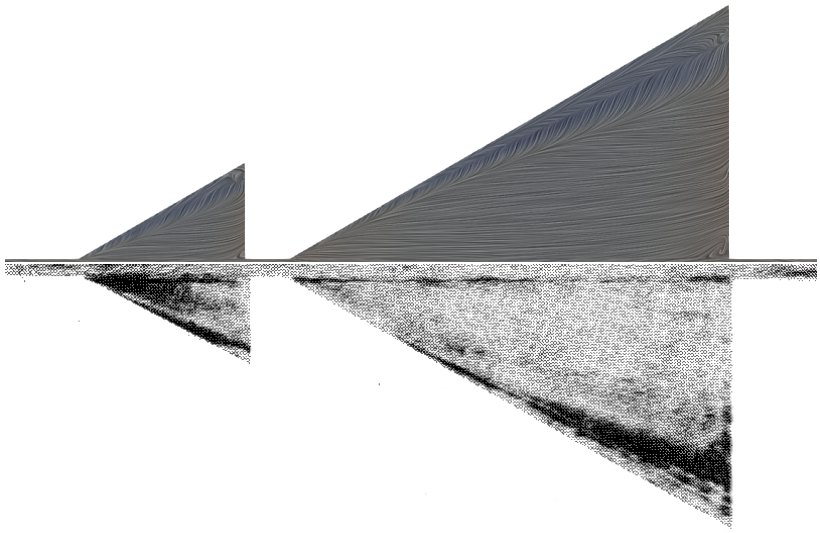

Figure 3.14: Oil flow visualization from experiment[50] and calculated surface streamlines, $\alpha = 8.7°$

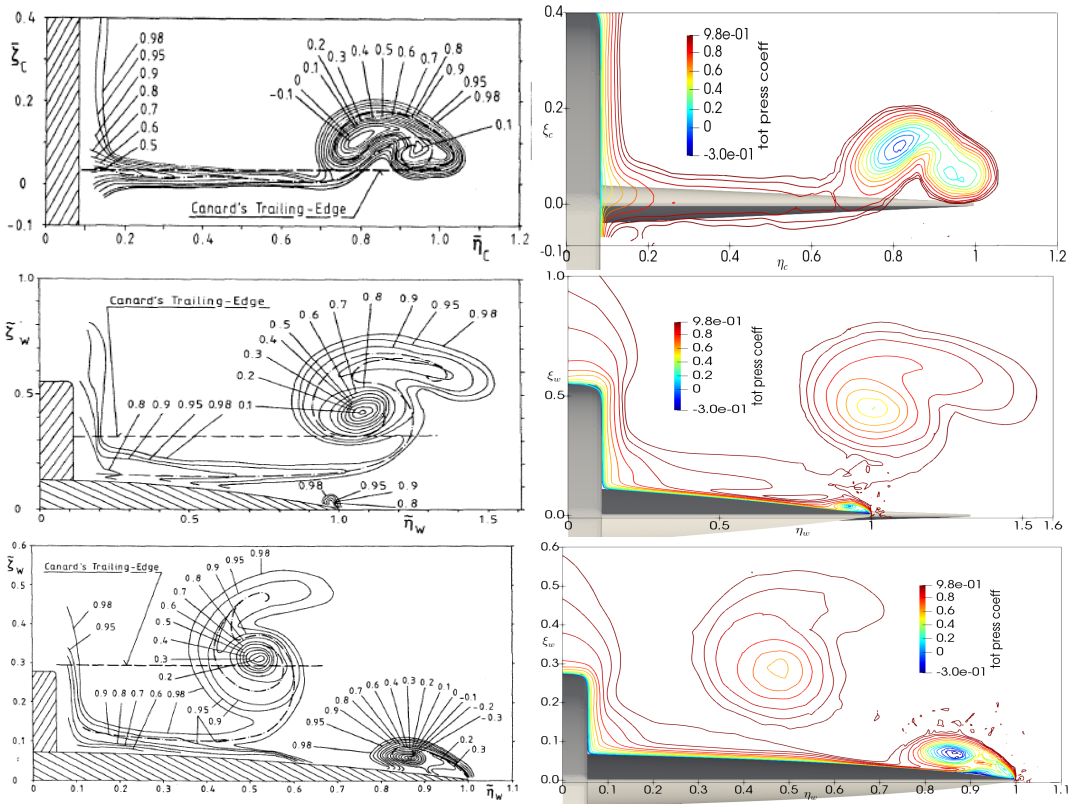

Figure 3.15: Total pressure coefficient contours, measurements [50] and calculations at $x/c = 0.0,\ 0.30,\ 0.60$, $\alpha = 8.7°$

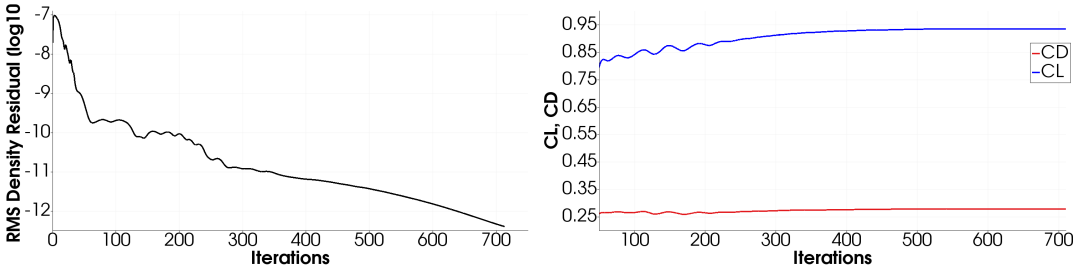

Figure 3.16: Convergence history of flow solution, canard-on case $\alpha = 20°$

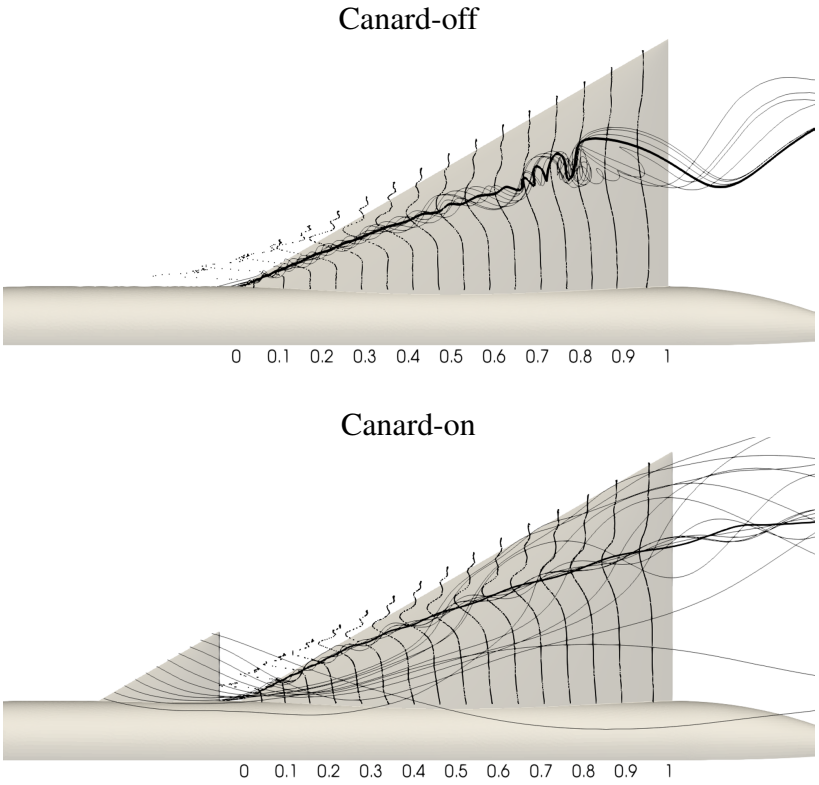

Figure 3.17: Wing surface pressure distributions and vortex core streamlines, $\alpha = 20°$

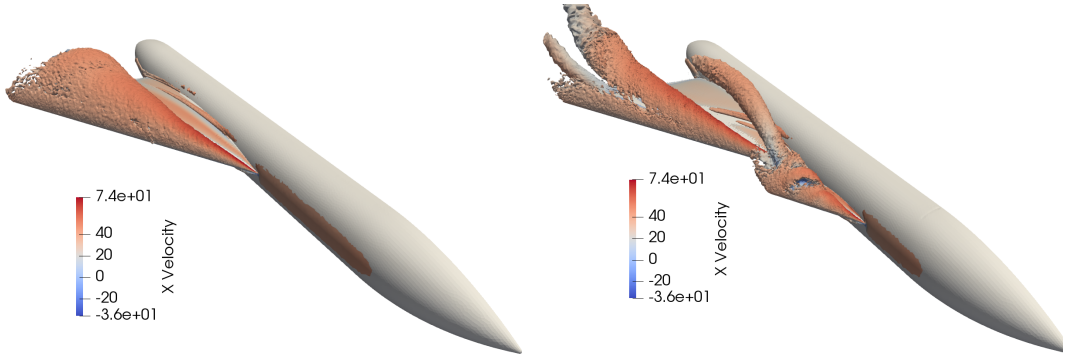

Figure 3.18: Q-criterion contours on canard-off and canard-on configurations, $\alpha = 20°$

at $\alpha = 20°$, first. Flow structure, surface pressure distributions and integrated force coefficients are used both to compare the calculations to measurements and to make further evaluations on vortex dynamics. In order to get a reasonable convergence, density residual reduction by five-order is achieved. C_L and C_D values are also converge throughout the iterations, seen in figure 3.16, and then flow field solutions are examined.

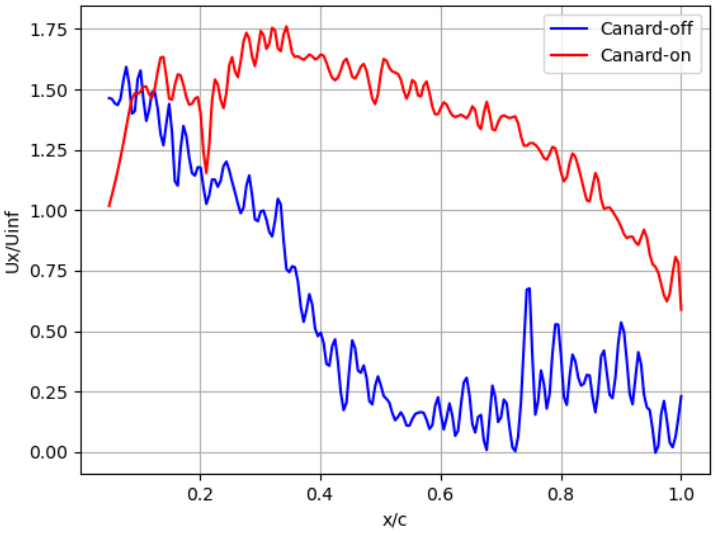

Figure 3.19: Axial velocity in wing vortex core, $\alpha = 20°$

Figure 3.17 compares canard-off and canard-on configurations by means of wing vortex core streamlines and wing span-wise surface pressure distributions. On both configurations, wing vortex cores move along a straight path, as represented by streamlines, and C_P distribution plots show a similar path for peak locations. Those peaks seen in C_P plots are suction peaks and are resulted from the low pressure due to wing vortex. On canard-off configuration, there exists a sudden expansion and a swirl in core streamlines, at $x/c \approx 0.80$ location. It indicates that there exists vortex bursting which is caused by breakdown. However, on the canard-on configuration, streamlines do not exhibit such swirling flow motion. In other words, canard prevents the wing vortex from a breakdown over the wing.

Breakdown location can be identified by plotting chord-wise axial velocity distribution of wing vortex. Figure 3.19 shows the axial velocities at wing vortex cores of both

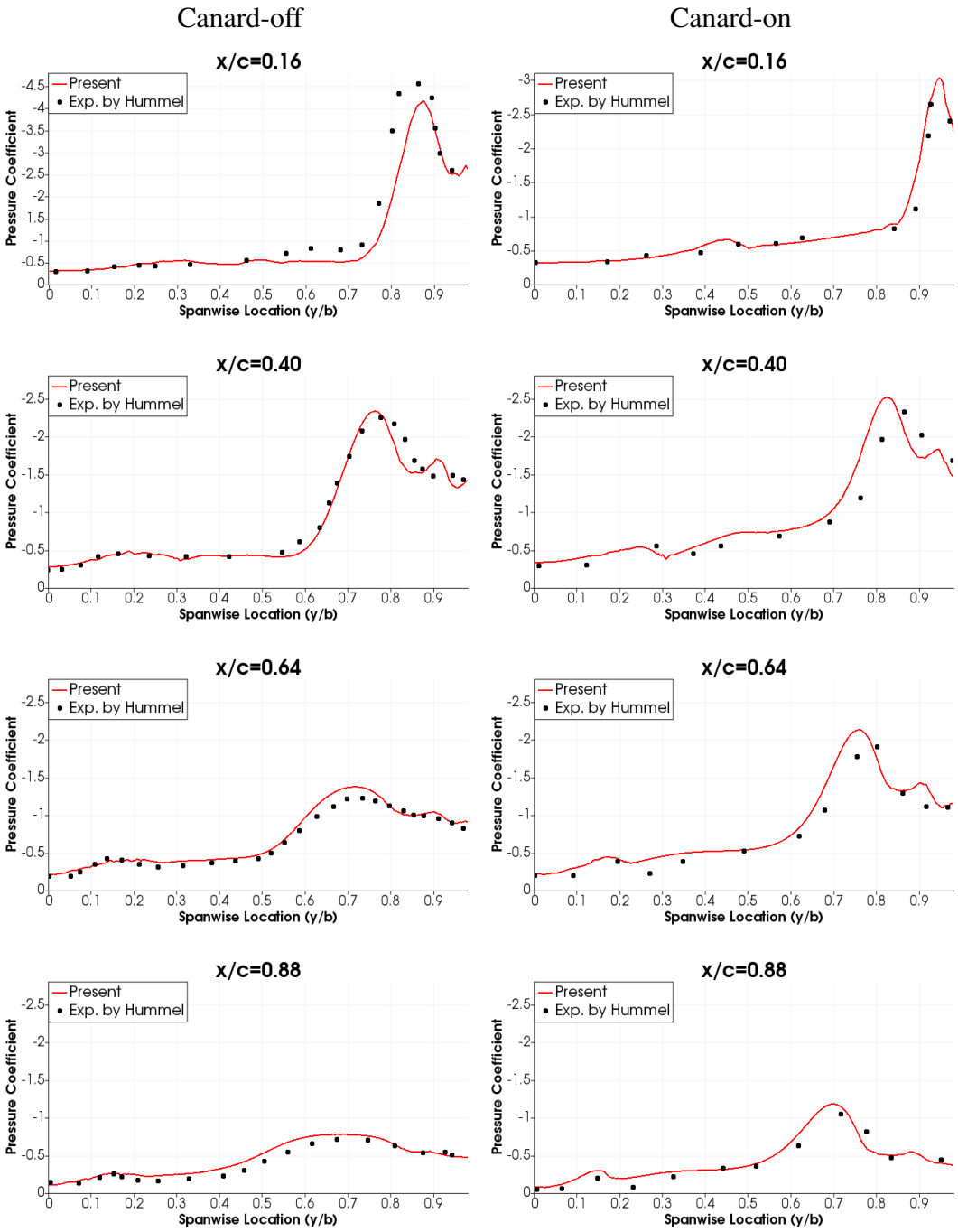

Figure 3.20: Surface pressure distributions, calculations and measurements [4], $\alpha = 20°$

canard-on and canard-off configurations. Axial velocities are non-dimensionalized by free-stream velocity magnitude and plotted along the chord-wise locations over the wing. Since a vortex breakdown is identified by a sudden lost of the jet-like axial velocity, the most upstream point that reach the zero axial velocity shows the breakdown location, and further, negative axial velocities represent the reversal flow regions. Figure 3.19 provides a more accurate observation on breakdown location which is discussed in the previous paragraph. On canard-off configuration, vortex breakdown exists before $x/c = 0.80$, at approximately $x/c = 0.70$. On the other hand, application of canard to the configuration provides much higher, or preserved, axial velocity in wing vortex core and breakdown is eliminated on wing.

Figure 3.18 shows vortex dynamics on both canard-off and canard-on configurations by q-criterion of vorticity iso-surfaces over canard and wing. A relatively narrow vortex cone is seen on canard-on configuration. One can interpret it as the downwash effect of canard on wing effective angle of attack. In addition Yutuk et al. [76] observed that the presence of the canard vortex over the wing keeps the wing vortex from expanding towards the wing root and losing its strength. Another remarkable observation which q-criterion iso-surfaces reveal is that canard vortices breaks down at this angle of attack and it shows a bubble-type flow structure at the canard trailing edge and in region between canard and wing. However, in the vicinity of the wing apex and the further downstream, due to the acceleration of the flow caused by wing, broken down canard vortex is recovered again and appears as an ordinarily structured vortex flow. This phenomenon has been already demonstrated in literature.

In figure 3.20 span-wise C_P distribution at four selected wing sections are plotted in order to evaluate the suction regions in detail. One can see that at the vicinity of wing apex, canard-on configuration generates a weaker suction, due to the well-known effect of canard downwash. On the other hand, although it works in a less effective angle of attack, canard-on configuration reaches and even overtakes the suction peak value of canard-off configuration at $x/c = 0.80$. Further downstream, favorable effect of canard upwash preserves the wing vortex throughout the wing, while a sudden decrease on suction peak value, in other words the breakdown, exists on canard-off configuration. These C_P plots also show that numerical solutions predict a secondary vortex region, as expected, at about $y/b = 0.90$ on both canard-off and canard-on con-

figuration. An additional weaker suction peak is seen at the wing inboard throughout the wing. According to Bergmann et al. [4] this suction peak is due to the formation of fuselage vortex. One can observe that fuselage vortex moves closer to primary wing vortex by comparing the relevant suction peak on pressure plots at 3.20 and 3.11.

3.4.3 Canard-Wing configuration at $\alpha = 30^{\circ}$

The flow over canard-on and canard-off configurations at $\alpha = 30^{\circ}$ is evaluated by means of the same flow properties evaluated in $\alpha = 20^{\circ}$. Similar to previous cases, those flow properties are examined after a five-order reduction in root-mean-square density residual is satisfied (figure 3.21). Since $\alpha = 30^{\circ}$ case is already considered in verification studies detailed span-wise C_P distribution plots on the selected four sections are not repeated here. Instead, vortex trajectories and interactions are evaluated mainly.

The C_P distributions in figure 3.22 shows a dead-water-like flow structure with reduced suction region and flattened span-wise pressure distribution on most of the wing, in canard-off case. The streamlines passing through the vortex core, consistently, exhibit a chaotic vortex-core flow which moves downstream and then back to upstream and at the same time swirl around a wide region. These flow dynamics are seen behind the vortex breakdown and therefore it is observed that breakdown occurs at a location, close to wing apex, at about $x/c \approx 0.25$, in canard-off case. Whereas in the canard-on configuration canard vortex induced the wing flow and breakdown location is delayed to $x/c \approx 0.80$ location.

Similar to figure 3.22, figure 3.24 also shows a dramatic improvement provided by canard. In this figure, axial velocity distribution of canard-off case reveals reversal flow at a location very close to wing apex and burst flow behavior shown by core streamlines in figure 3.22 is seen as an oscillatory velocity plot in this figure. On the other hand, in canard-on configuration, wing vortex axial velocity reaches zero at further downstream, at $x/c \approx 0.75 - 0.78$, compared to canard-off configuration.

Similar to $\alpha = 20^{\circ}$ case, 3.23 shows that canard vortex recovered by the acceleration

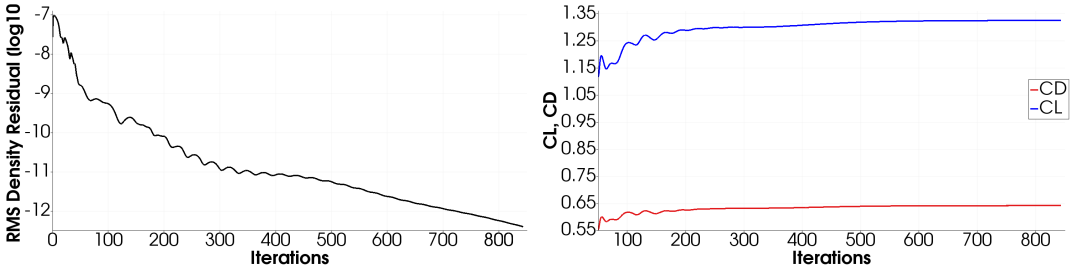

Figure 3.21: Convergence history of flow solution, canard-on case $\alpha = 30°$

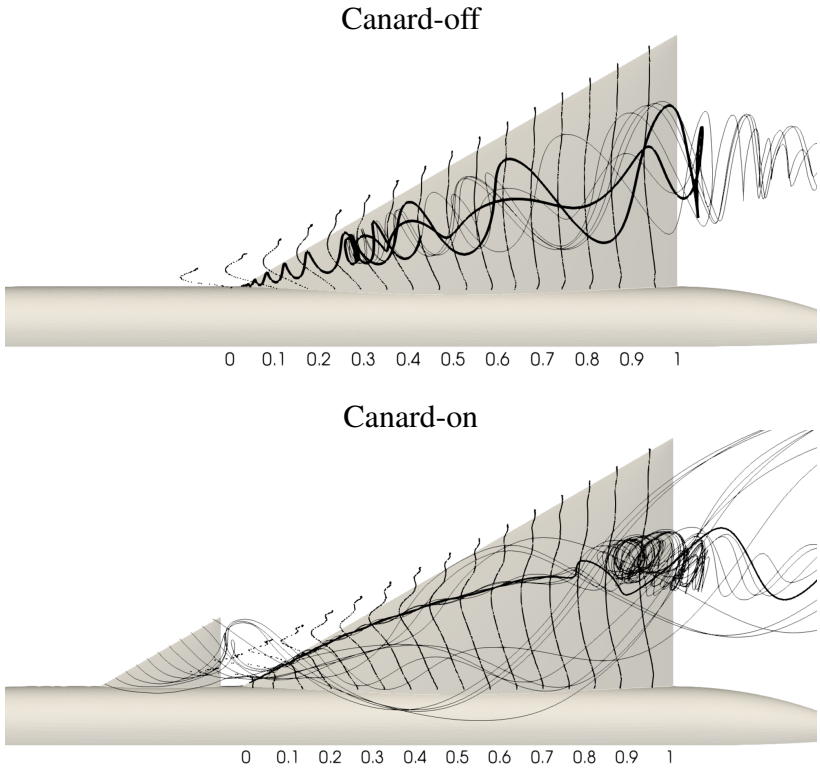

Figure 3.22: Wing surface pressure distributions and vortex core streamlines, $\alpha = 30°$

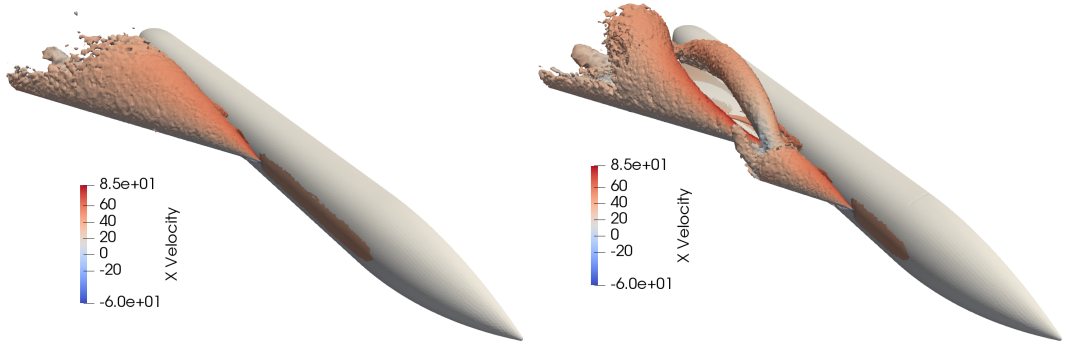

Figure 3.23: Q-criterion contours on canard-off and canard-on configurations, $\alpha = 30°$

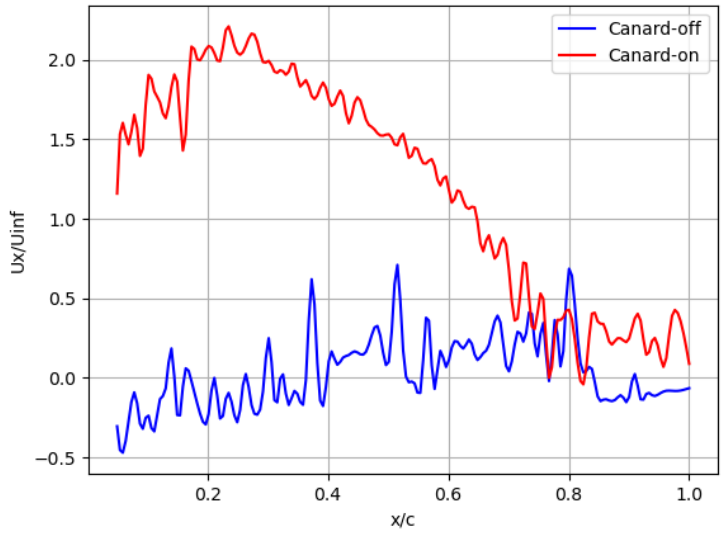

Figure 3.24: Axial velocity in wing vortex core, $\alpha = 30^{\circ}$

of flow due to the existing of wing, although the canard vortex is already burst. It is observed that canard vortex preserves the wing primary vortex as long as canard vortex dissipates. It is seen in the right figure of figure 3.23 wing vortex suddenly expands when canard q-criterion iso-surface diminishes. Another notable observation is the trajectories of vortices. Canard vortex moves downward and outboard over the wing, while the wing vortex is pushed upward and moves toward inboard over the wing.

3.4.4 Effect of Canard on Aerodynamic Forces

The effect of canard on the integrated aerodynamic forces are given in table 3.2. For both configurations and both angle of attack cases, predicted lift and drag values are in a very good agreement with the measurements. The predictions show that canard-wing configuration having a coplanar layout provides a lift increment by about 12% at $\alpha = 20^{\circ}$ and 16% at $\alpha = 30^{\circ}$, while adding a new lifting surface increases the drag by about 10% and 14%, respectively. One should bear in mind that canard-on configuration is more effective, and efficient, at high angles of due to the fact that canard contributes in lift increment not only by providing an additional lifting surface

Table 3.2: Effect of canard on the lift and drag coefficients (C_{Lw} for wing and C_{Lc} for canard contribution)

	Canard-off				Canard-on				
α	C_{Lw}	C_L	$C_L Exp.$[4]	C_D	C_{Lw}	C_{Lc}	C_L	$C_L Exp.$[4]	C_D
20°	0.637	0.824	0.84	0.248	0.647	0.070	0.935	0.92	0.279
30°	0.792	1.108	1.11	0.544	0.864	0.111	1.325	1.33	0.642

but also by preventing the wing vortex breakdown of which has much dramatic effect at higher angles of attack.

3.5 Optimization Studies

As stated in previous sections, the optimization problem is based on an experimental study of Oelker et al. [50]. Therefore the geometry (see figure 3.1b), identical to experiment is subjected to flow conditions of 0.177 Mach and $Re = 1.4 \times 10^6$, at two angles of attack, $\alpha = 8.7°$ and $\alpha = 20°$. Objective function is C_L while the canard is translated along horizontal and vertical axes.

Translation of canard is provided by an FFD box enclosing the canard surface (see figure 3.25a). Eight vertex points of box are the control points and therefore 16 design variables are defined for this technique, they are allowed to move in x and z axes. In order to move the canard as a rigid body, all those control points move together. This final translation vector is an average of gradients of separate deformations of control points. The FFD box is also surrounded by outer FFD boxes as seen in figure 3.25b Outer boxes are needed to be defined in a such strategy so that the mesh deformation due to the translation of main box is distributed to those outer boxes and damped throughout them.

3.5.1 Configuration Optimization at $\alpha = 8.7°$

Optimization problem is employed to Oelker's close-coupled canard-wing configuration (figure 3.1b), which is called as baseline geometry from now on, at the same

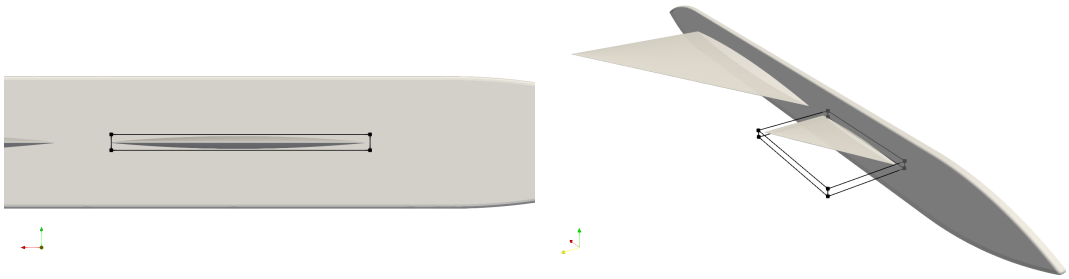

(a) Main FFD box enclosing the canard surface

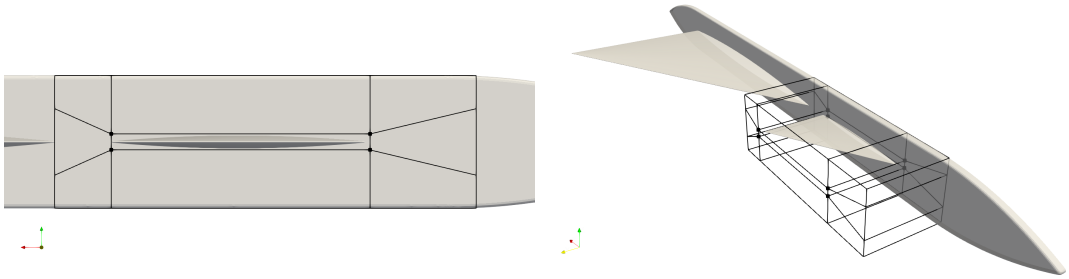

(b) Outer FFD boxes enclosing the main FFD box

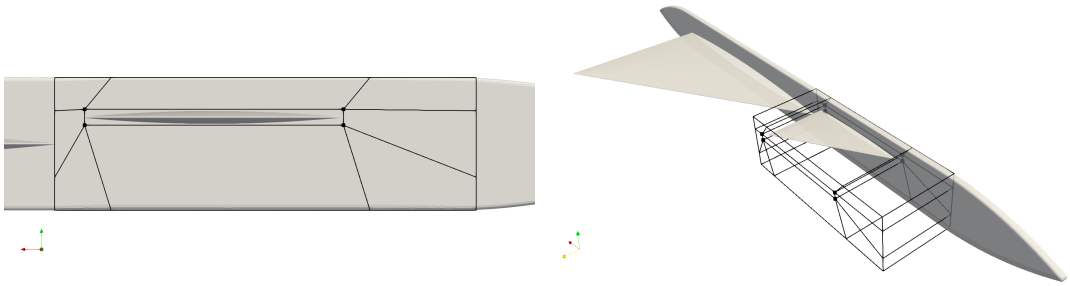

(c) Translation of canard via translation of control points and deformations on FFD boxes

Figure 3.25: FFD boxes enclosing the translated canard surface

conditions with the experiment [50]. Optimization process translates the canard to upward and closer to the wing, as expected from the literature survey. Variations in objective function, C_L, and design variables, translation amounts in x and z directions, are given in figures 3.26 and 3.27, respectively, and a comparison between baseline and optimized canard positions is given in figure 3.28. Due to the geometric boundaries and limited flexibility of mesh deformation technique, canard translation on both directions are limited to ± 25 mm.

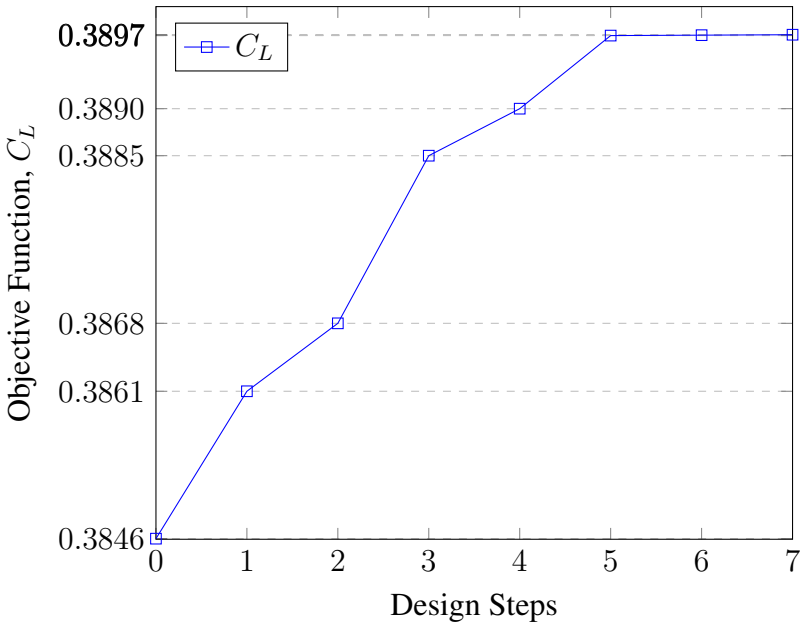

Figure 3.26: Variation of objective function, $\alpha = 8.7°$

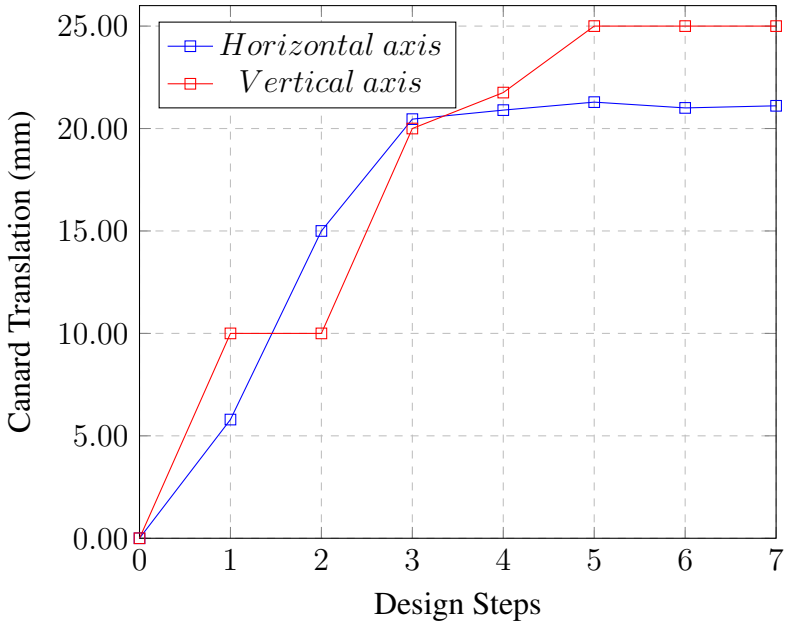

Figure 3.27: Translation amounts of design variables, $\alpha = 8.7°$

As observed, through the first three design steps design variables and objective function rapidly change, and at step 5, objective function reaches its converged value. The optimization process leads an increment in C_L by only 1.32%. But, previous studies in literature state that at such low angles canard and wing vortices exhibit a limited interaction. Therefore, at this angle of attack, small increments in objective function

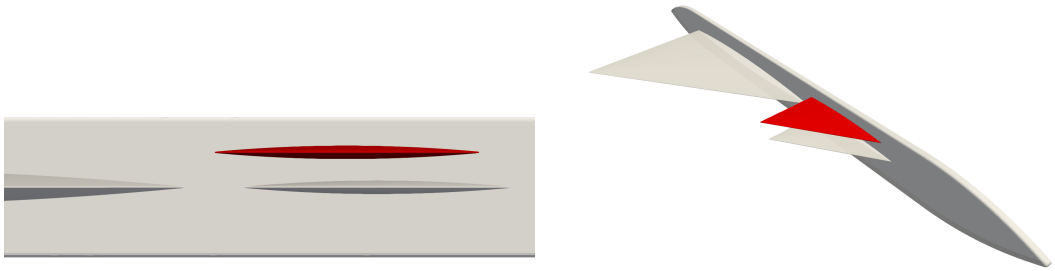

Figure 3.28: Canard positions on baseline and optimized geometry, $\alpha = 8.7°$

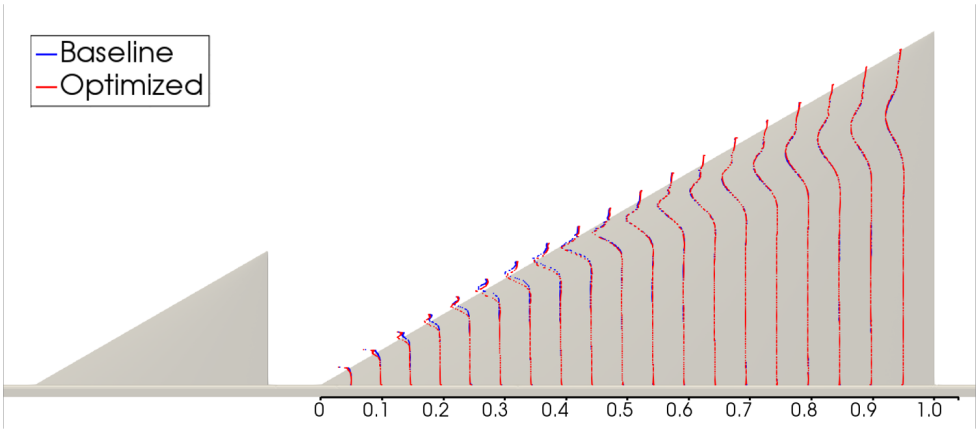

Figure 3.29: Surface pressure distributions of baseline and optimized geometries, $\alpha = 8.7°$

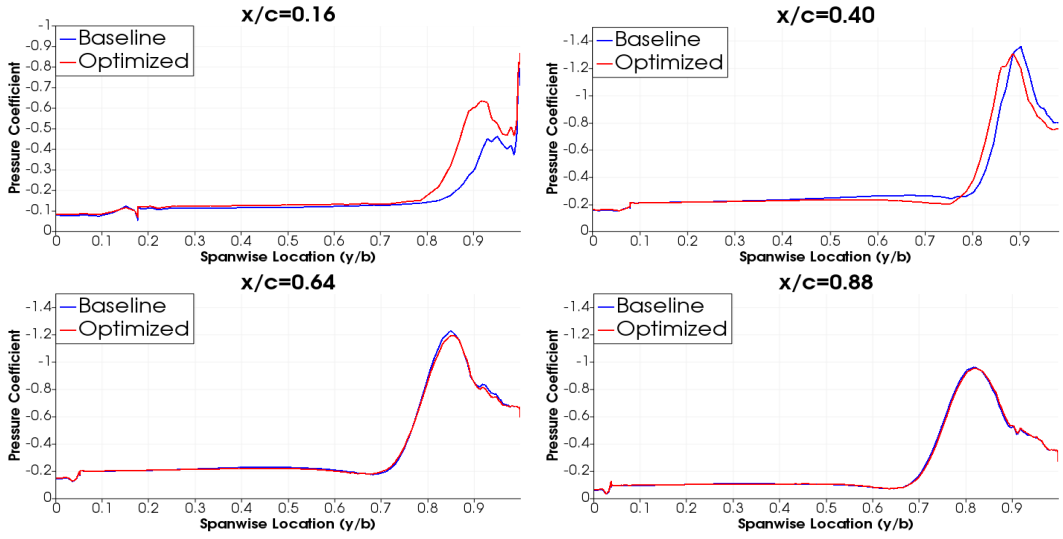

Figure 3.30: Surface pressure distributions of baseline and optimized geometries, $\alpha = 8.7°$

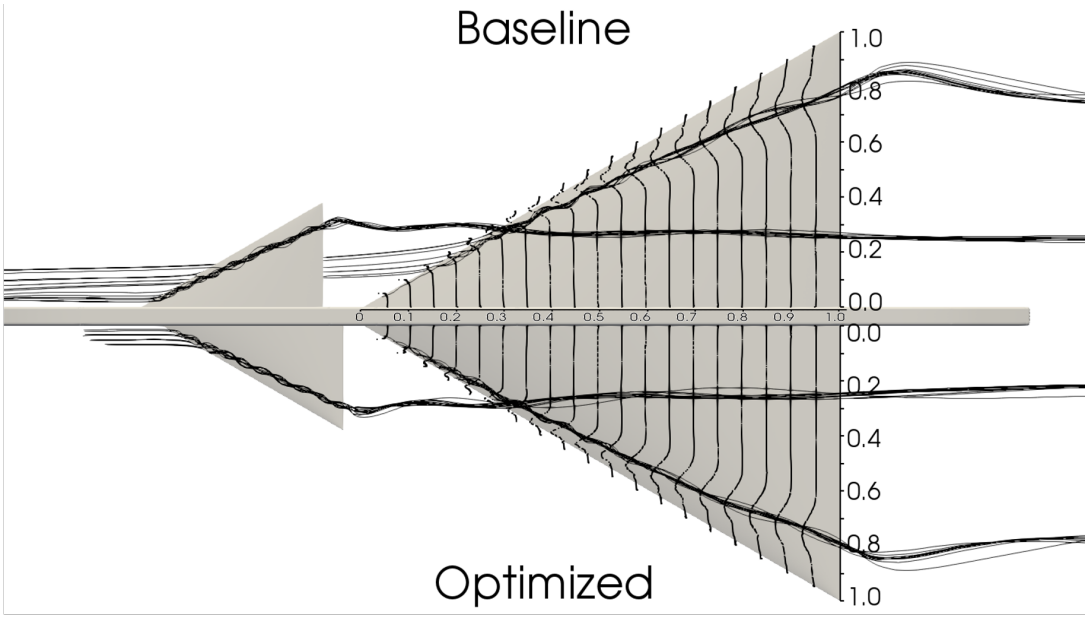

Figure 3.31: Wing surface pressure distributions and vortex core streamlines on baseline and optimized geometries, $\alpha = 8.7°$

is still acceptable. Meanwhile, canard position is reached to the boundary in z direction and approached considerably to the boundary in x direction. One can observe a correlation between the vertical position of canard and the objective function. It seems that vertical position of canard has a dominant effect on C_L, rather than its horizontal position. Therefore, besides the low angle of attack, geometric boundary is seemed to be a limitation for a higher lift increment in this case. On the other hand, this translation of canard surface increases the positive moment in y direction from $C_{M_y} \approx 0.012$ to $C_{M_y} \approx 0.013$ which results an 8.8% increase in pitch-up moment. One should keep in mind that moment is not constrained in this study, but it can be employed into the problem as a linearity or non-linearity constraint if its changes are somehow wanted to be limited.

The turbulent flow fields are compared for baseline and optimized geometries in terms of surface pressure distributions, vortex core streamlines, and q-criterion contours. In figures 3.29 and 3.30, a stronger suction region, in other words higher suction peaks in C_p distributions, is observed in the forward section of wing up to $x/c = 0.40$. At the downstream of $x/c = 0.40$, on the other hand, pressure distributions of two configurations are almost identical. When the vortex core streamlines are observed in

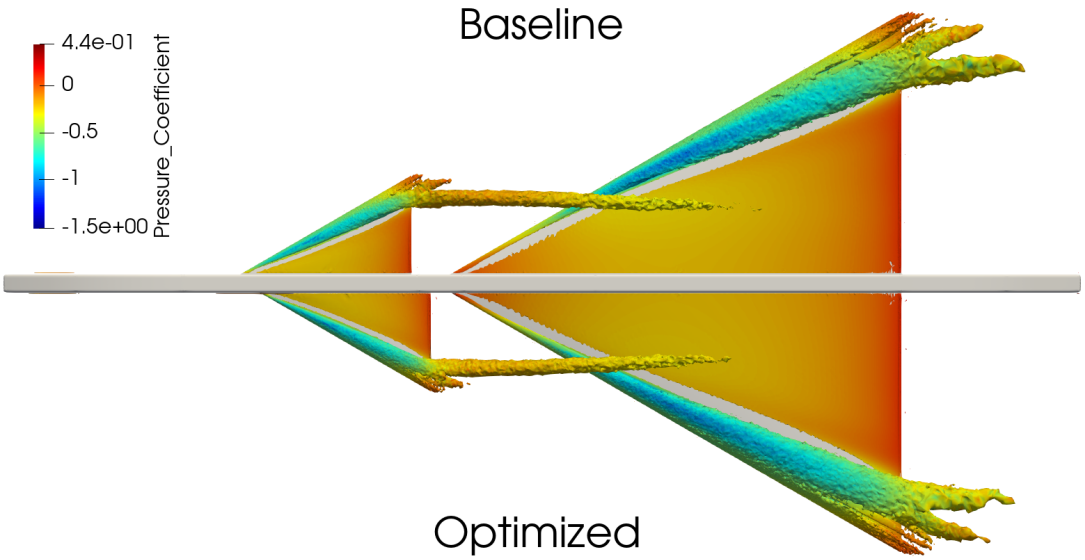

Figure 3.32: Q-criterion contours on baseline and optimized geometries, $\alpha = 8.7°$, upper view

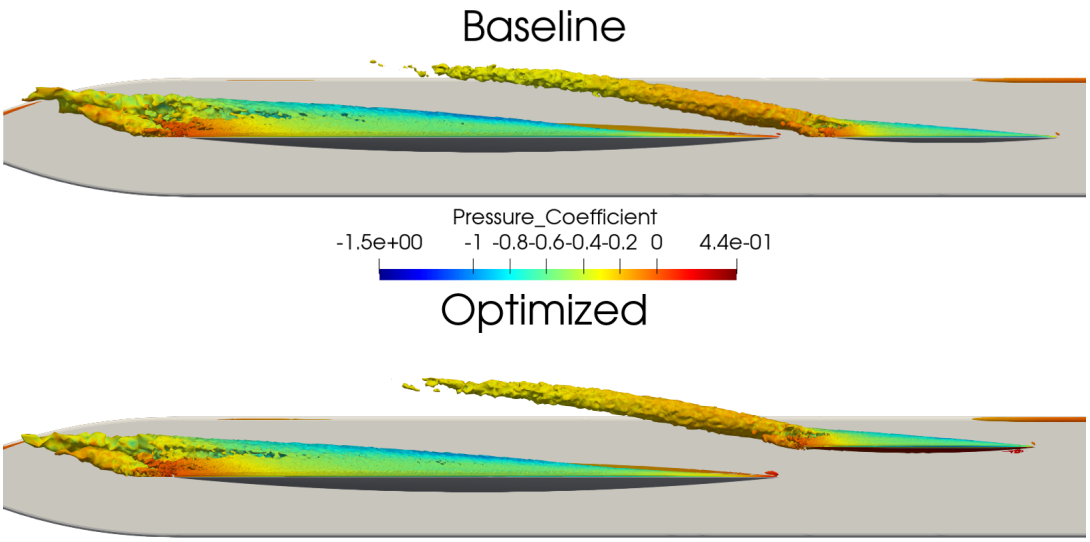

Figure 3.33: Q-criterion contours on baseline and optimized geometries, $\alpha = 8.7°$, side view

figure 3.31, it is seen that canard vortex crosses over the wing surface at $x/c = 0.40$. Previous studies show that canard vortex has a downwash effect on the wing portion which is inboard of the canard vortex and as it is seen in figure 3.31, the wing portion at the upstream of $x/c = 0.40$ is exposed to this downwash effect. It seems that vertical position of the canard leads to a reduction in this downwash effect at the

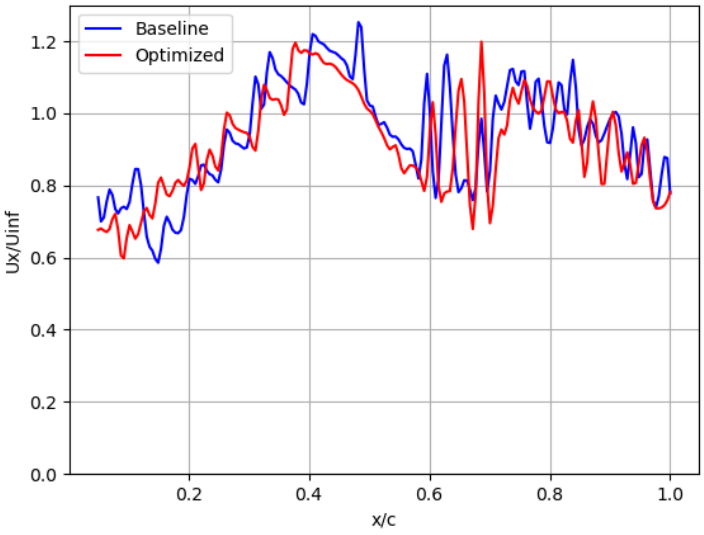

Figure 3.34: Axial velocity in wing vortex core, $\alpha = 8.7°$

upstream portion of the wing at optimized geometry and thus an increase in suction peaks at the sections $x/c < 0.40$. On the other hand, at $\alpha = 8.7°$, vortex trajectories in the horizontal plane are identical for both configurations; both wing vortices leaves the wing at the location of $y/b = 0.80$, both canard vortices cross over the wing vortex at $x/c \approx 0.35$. move in a straight path and leave the wing geometry at $y/b \approx 0.25$. Therefore, for both configurations, the effect of canard vortex on the flow over wing becomes identical at the downstream of location $x/c = 0.40$.

The observations discussed in above paragraph can be expanded by a qualitative comparison of q-criterion contours in figures 3.32 and 3.33. In figure 3.32 q-criterion contours and vortex trajectories are identical for both configurations. On the other hand, it is seen in figure 3.33 that canard vortex is translated away from the wing vortex region. It seems that, as a result of this divergence of two vortex regions, the downwash effect of canard vortex at the upstream portion of wing is reduced and thus, suction is increased.

The further inspection on wing vortex axial velocity plot (figure 3.34 repeats the observations stated above paragraphs. Throughout the wing portion of $x/c < 0.40$, optimized geometry reveals slightly higher axial velocity magnitude, which is related to the stronger suction force at this region. At the downstream axial velocity plots

have the same trend for both configurations. At this angle of attack vortex breakdown does not occur and wing vortex preserves its strength throughout the wing.

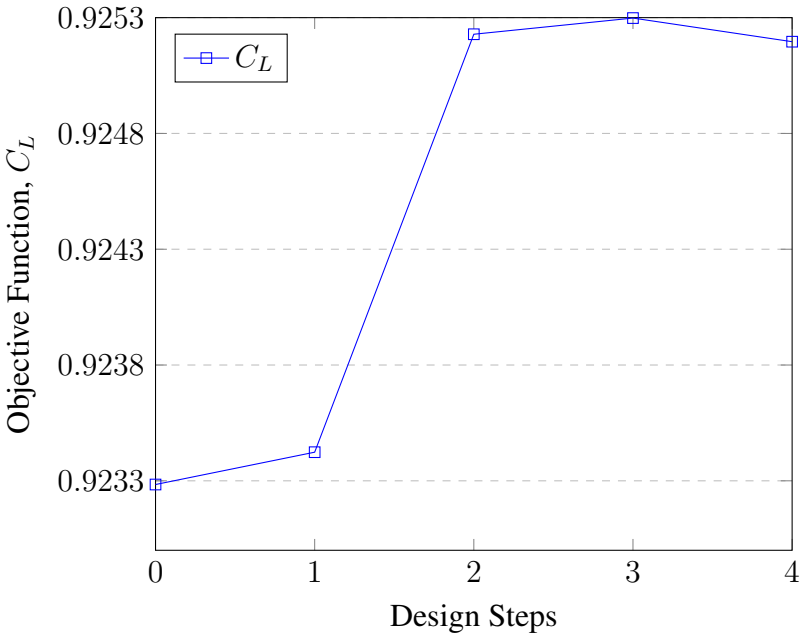

Figure 3.35: Variation of objective function, $\alpha = 20°$

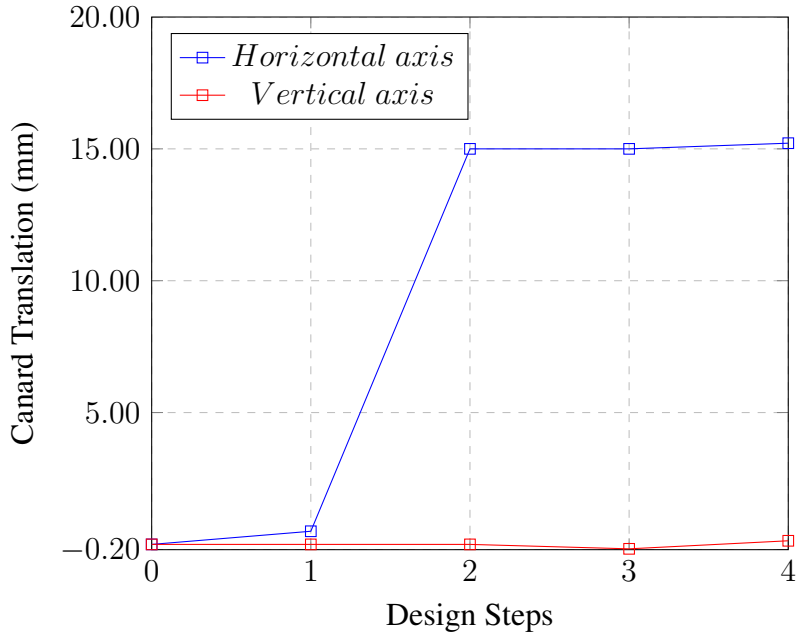

Figure 3.36: Translation amounts of design variables, $\alpha = 20°$

3.5.2 Configuration Optimization at $\alpha = 20°$

A further optimization case is employed to the same geometry, but this time at $\alpha = 20°$. Figures 3.35 and 3.36 show variation of objective function and design variables, in this case. The optimization process achieves a significant canard translation in +x direction, i.e. canard is translated closer to the wing surface. On the other hand, almost no change is applied in vertical direction. This horizontal translation leads an improvement in C_L about 0.22%. In previous case, it is seen that there is a strong correlation between vertical translation amount and the increment in objective function. Similarly, figures 3.35 and 3.36 show that the effect of canard's horizontal translation does not have a significant effect on C_L, at least for a configuration of which canard and wing is in coplanar layout. On the other hand, this final position, which is translated mainly in horizontal direction, results 13% reduction in pitch-up moment. The effect of canard's horizontal translation on pitch-up moment can be seen in figure 3.37. Therefore, it is resulted that horizontal position mainly effects the pitch-up moment, while lift almost does not change.

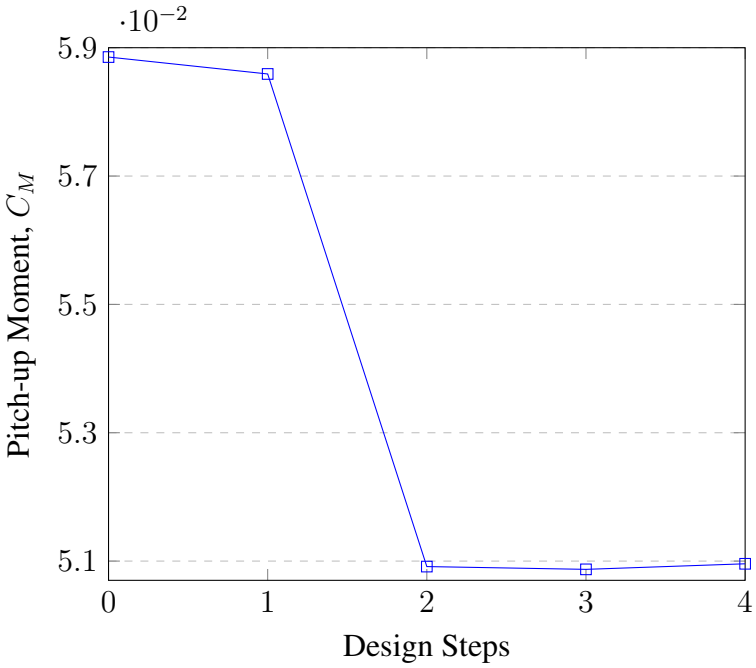

Figure 3.37: Variation of pitch-up moment, $\alpha = 20°$

When span-wise C_P distribution plots over the wing are examined in detail, it is seen that, over the upstream portion of wing, up to $x/c \approx 0.40$, suction peak is slightly

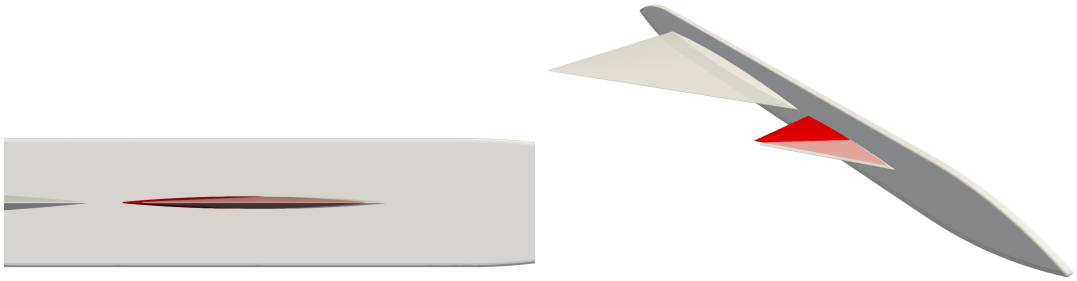

Figure 3.38: Canard positions on baseline and optimized geometry, $\alpha = 20°$

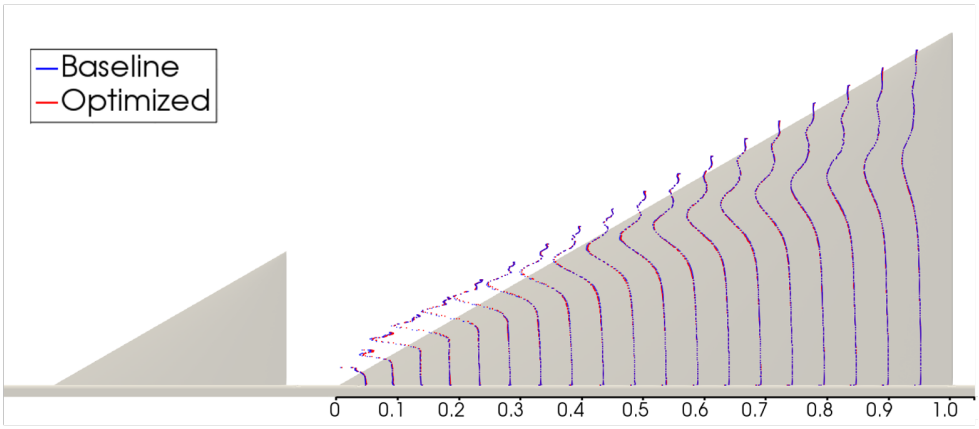

Figure 3.39: Surface pressure distributions of baseline and optimized geometries, $\alpha = 20°$

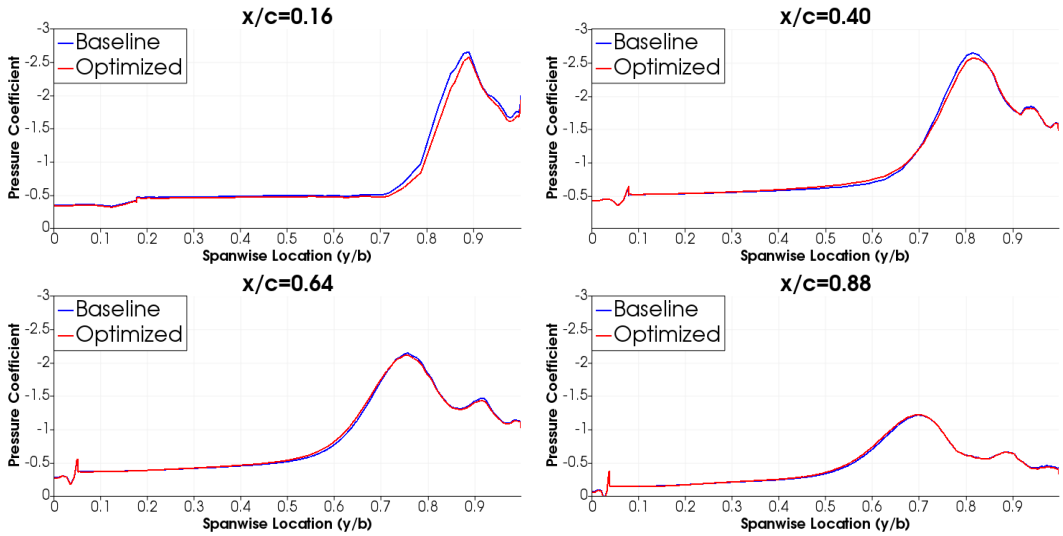

Figure 3.40: Wing surface pressure distributions of baseline and optimized geometries, $\alpha = 20°$

weaker for optimized geometry. Translating the canard in horizontal direction closer to wing increases the downwash effect of the canard which leads to weaker wing leading edge vortex on this upstream portion of the wing. On the other hand, at further downstream, upwash of canard vortex provides recovering the suction force, as seen at $x/c = 0.88$ in figure 3.40.

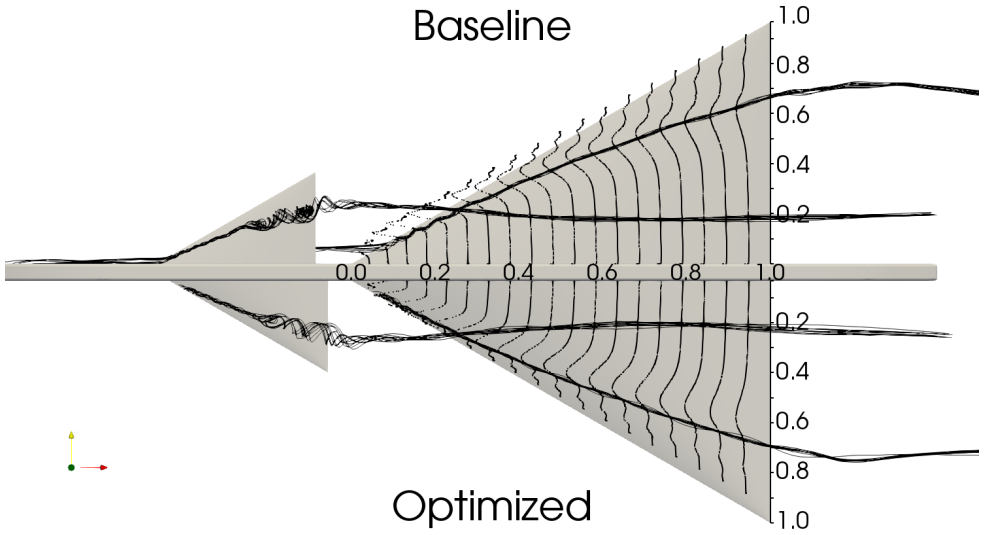

Figure 3.41: Wing surface pressure distributions and vortex core streamlines on baseline and optimized geometries, $\alpha = 20°$

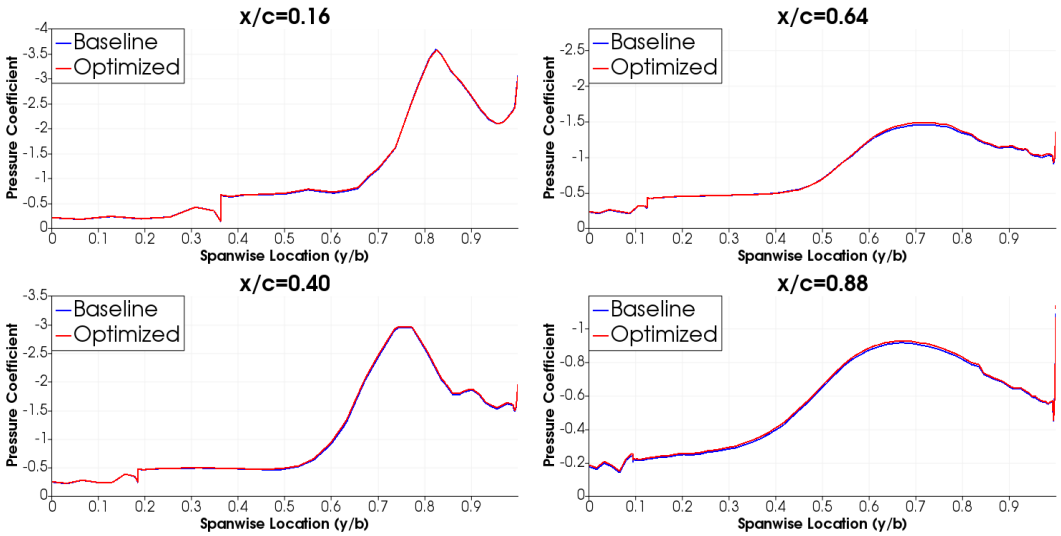

Figure 3.42: Canard surface pressure distributions of baseline and optimized geometries, $\alpha = 20°$

It is also a well-known phenomenon that the favorable pressure gradient induced by

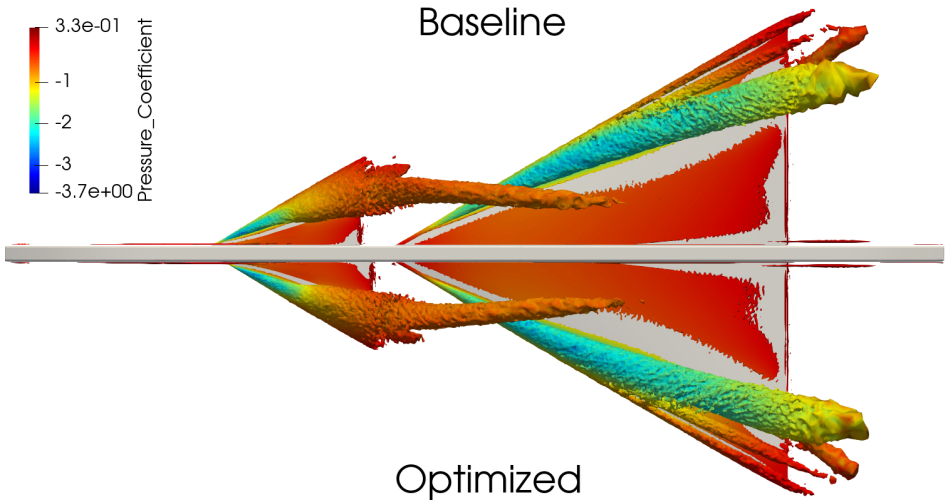

Figure 3.43: Q-criterion contours on baseline and optimized geometries, $\alpha = 20°$, upper view

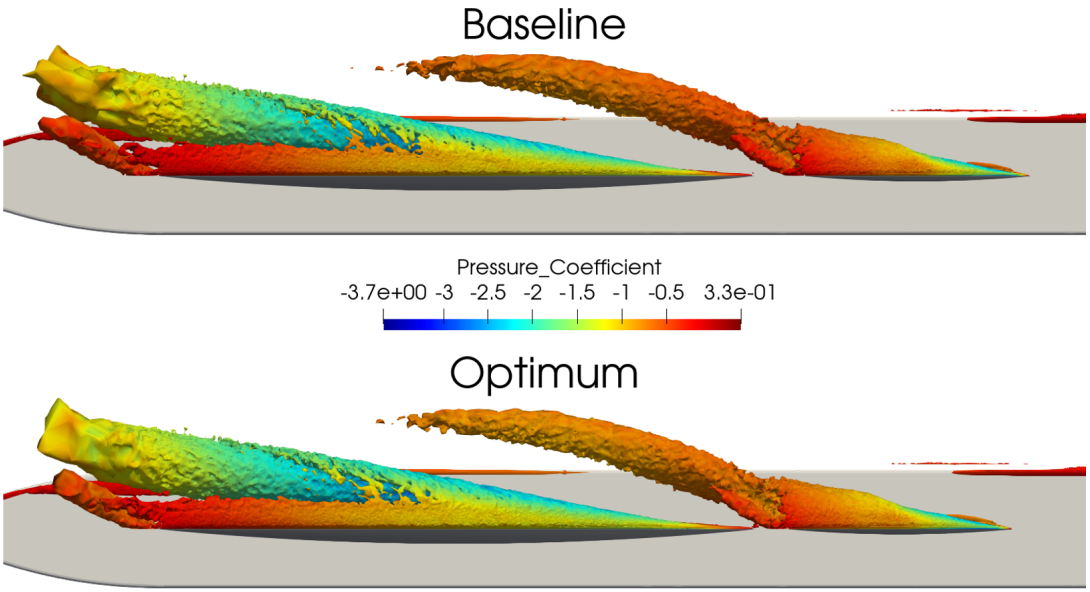

Figure 3.44: Q-criterion contours on baseline and optimized geometries, $\alpha = 20°$, side view

wing provides restoring the canard vortex into a non-burst state (see [32]). Therefore it seems that moving canard closer to the wing is not only effects flow over wing, but also favorably effects the state of canard vortex. It is seen in figure 3.41 that canard vortex breakdown in baseline geometry results a much chaotic burst flow region. However, in optimized geometry, although canard vortex is also burst, swirling

canard vortex core streamlines keep moving in a relatively straight path along the vortex trajectory. As the result, a slight increase in suction region is seen at sections $x/c = 0.64$ and $x/c = 0.88$ on the canard, in figure 3.42.

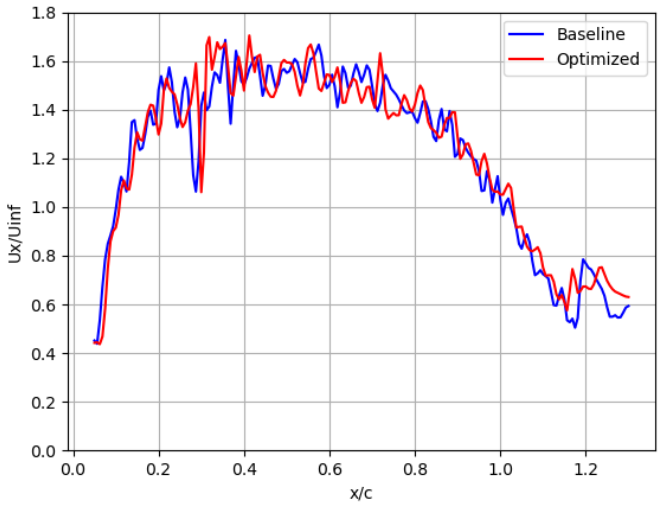

Figure 3.45: Axial velocity in wing vortex core, $\alpha = 20°$

Table 3.3: Lift increment due to configuration optimization, $\alpha = 20°$

	C_{L_c}	C_{L_w}	Total C_L
Baseline	0.1220	0.7539	0.9234
Optimum	0.1239	0.7544	0.9252

A qualitative comparison of vortex trajectories of the two geometries by q-criterion iso-surface plots and a quantitative comparison by axial velocity plot are given in figures 3.43,3.44 and 3.45, respectively. For this case, the slight changes in vortices due to horizontal translation of canard can not be seen clearly. The axial velocity plot clarifies this slight variation in the strength of wing vortex due to optimization. At upstream region, axial velocity of the baseline geometry's vortex is slightly higher up to $x/c \approx 0.3$. Near the trailing edge, and further downstream optimized geometry reveals slightly higher axial velocity.

To summarize the above results the lift and drag coefficient components from wing and canard, and the total values are gathered together in the table 3.3. As seen, the

most of the increment in C_L is provided by the canard, which is about 1.55%, while lift increment over wing is only 0.07%. So, it seems that, for this case, effect of the wing flow on the canard vortex has a higher impact on lift increment rather than the effect of canard vortex on the wing flow.

CHAPTER 4

CONCLUSION

In this thesis, vortical flow field over a close-coupled canard-wing configuration is investigated, including vortex interaction and vortex breakdown mechanisms, and an optimization framework is introduced, based on gradient-based optimization technique coupled with adjoint method, to improve aerodynamic performance of the configuration. An open-source finite volume CFD solver, SU^2 and an open-source optimization toolkit, DAKOTA, are employed to construct the framework and used in the optimization problems to improve the lift coefficient, C_L, of a close-coupled canard-wing configuration. Design variables are determined as horizontal and vertical locations of canard and translation is provided by a free-form deformation box enclosing the canard geometry. The grid is also deformed by a set of free-form deformation boxes around the canard geometry in order to eliminate need of re-meshing at each design step. Sensitivity derivatives with respect to design variables are obtained by discrete adjoint solver of SU^2.

Flow solutions are first subjected to verification studies. These verification studies indicate that Menter's SST turbulence model and one-step-adapted grids, which are adapted by a solution-based adaptive grid refinement technique, provide predictions in good agreements with experimental measurements, in terms of vortex breakdown locations and vortex induced aerodynamic loads. Then characteristics of such vortical flows and vortex interactions are investigated at low-, moderate- and high-angle-of-attack cases, $\alpha = 8.7°,\ 20°,\ 30°$ respectively. It is resulted that at low angles of attack vortex interactions are limited, however as the angle of attack increase the effect of canard vortex becomes significant. Wing vortex breakdown is completely eliminated at $\alpha = 20°$ and it is delayed from $x/c \approx 0.25$ to $x/c \approx 0.85$ at $\alpha = 30°$ due to the

presence of canard vortex. As a result, an increment of 12% and 16% in total C_L is provided by canard implementation, respectively at $\alpha = 20^\circ$ and $\alpha = 30^\circ$.

Then, configuration optimization process is employed to the canard-wing configuration in order to reach a further increment in C_L, at $\alpha = 8.7^\circ$ and $\alpha = 20^\circ$. Although the vortex interaction is limited at low angles of attack, C_L is improved by about 1.32% at $\alpha = 8.7^\circ$. The optimum canard location is determined in terms of relative position to its baseline location. The flow solution show that lift increment is provided by reducing the downwash effect of canard vortex which leads to an increase in suction peaks at the wing sections of $x/c < 0.40$.

The configuration optimization for $\alpha = 20^\circ$ case shows that horizontal translation of the canard does not have a significant impact on wing vortex as much as vertical translations. On the other hand, moving the canard closer to the wing has a positive effect on canard vortex, it provides recovering the burst canard vortex due to the favorable pressure gradient on the wing. As the result, only an increment in lift about 0.22% can be provided by this optimization process, whereas the most of this increase is provided by the flow over canard surface. On the other hand, 13% reduction in pitch-up moment, provided by this canard translation, shows that horizontal translation of canard has drastic effects on moment characteristics.

This study demonstrates that aerodynamic performance of a delta wing can be significantly enhanced by adding a canard surface in front of the wing in a close-coupled layout, especially at high angles of attack where the vortex breakdown is dominant over an isolated delta wing. Moreover, the aerodynamic performance can be enhanced even further by optimizing the canard-wing layout at a given condition. An adjoint-based optimization technique can be employed to such optimization problems which need to translate the whole geometry. However, this technique may further be improved by implementing a re-mesh step in the cycle since the deformation technique used in this study has a limited capability of handling such large amounts of geometry deformations. Also one can advance the problem by introducing the pitch-up moment well-known into the problem as an aerodynamic constraint, since it is well known that canard position considerably changes the longitudinal characteristics of the configuration.

REFERENCES

[1] N. Agrell and L. Elmeland. Transonic aerodynamic computations for a canard configuration. *Journal of Aircraft*, 22(8):675–678, 1985.

[2] H. Behrbohm. *Basic low speed aerodynamics of the short coupled canard configuration of small aspect ratio*. Svenska Aeroplan Aktiebolaget, 1965.

[3] A. Bergmann and D. Hummel. Aerodynamic effects of canard position on a wing body configuration in symmetrical flow. In *39th Aerospace Sciences Meeting and Exhibit*, page 116, 2001.

[4] A. Bergmann, D. Hummel, and H.-C. Oelker. Vortex formation over a close-coupled canard-wing-body configuration in unsymmetrical flow. *AGARD Conference Proceedings 494, Vortex Flow Aerodynamics 14 p(SEE N 92-12996 04-02)*, 1991.

[5] R. Biswas and R. C. Strawn. A new procedure for dynamic adaption of three-dimensional unstructured grids. *Applied Numerical Mathematics*, 13(6):437–452, 1994.

[6] R. Biswas and R. C. Strawn. Tetrahedral and hexahedral mesh adaptation for cfd problems. *Applied Numerical Mathematics*, 26(1-2):135–151, 1998.

[7] D. Bristow and J. D. Hawk. Subsonic panel method for the efficient analysis of multiple geometry perturbations. 1982.

[8] G. Butler. Effect of downwash on the induced drag of canard-wing combinations. *Journal of Aircraft*, 19(5):410–411, 1982.

[9] W. Calarese. Close-coupled canard-wing vortex interaction and reynolds stress acquisition. In *9th Atmospheric Flight Mechanics Conference*, page 1368, 1982.

[10] W. Calarese. Vortex interaction effects on the lift/drag ratio of close-coupled canard configurations. In *19th AIAA, Fluid Dynamics, Plasma Dynamics, and Lasers Conference*, page 1344, 1987.

[11] J. F. Campbell, B. B. Gloss, and J. E. Lamar. Vortex maneuver lift for supercruise configurations. 1976.

[12] M. Chen, P. Liu, H. Guo, and Q. Qu. Effect of sideslip on high-angle-of-attack vortex flow over close-coupled canard configuration. *Journal of Aircraft*, 53(1):217–230, 2016.

[13] A. Das and J. Longo. Numerical analysis of the vortical flow around a delta wing-canard configuration. *Journal of aircraft*, 32(4):716–725, 1995.

[14] J. Er-El. Effect of wing/canard interference on the loading of a delta wing. *Journal of Aircraft*, 25(1):18–24, 1988.

[15] J. Er-El and A. Seginer. The leading-edge vortex trajectories of close-coupled wing-canard configurations and their breakdown characteristics. In *Applied Aerodynamics Conference*, page 1817, 1983.

[16] J. Er-El and A. Seginer. Vortex trajectories and breakdown on wing-canard configurations. *Journal of Aircraft*, 22(8):641–648, 1985.

[17] L.-E. Eriksson and A. Rizzi. Computation of vortex flow around a canard/delta combination. *Journal of Aircraft*, 21(11):858–865, 1984.

[18] M. Ghoreyshi, A. Kim, A. Jirasek, A. Lofthouse, and R. Cummings. Validation of cfd simulations for x-31 wind-tunnel models. *The Aeronautical Journal*, 119(1214):479–500, 2015.

[19] B. B. Gloss. Effect of wing planform and canard location and geometry on the longitudinal aerodynamic characteristics of a close-coupled canard wing model at subsonic speeds. 1975.

[20] B. B. Gloss and L. W. Mckinney. Canard-wing lift interference related to maneuvering aircraft at subsonic speeds. 1973.

[21] B. B. Gloss and K. E. Washburn. Load distribution on a close-coupled wing canard at transonic speeds. *Journal of Aircraft*, 15(4):234–239, 1978.

[22] S. Goldstein and C. Combs. *Trimmed drag and maximum flight efficiency of aft tail and canard configurations*.

[23] R. E. Gordnier and M. R. Visbal. High-fidelity computational simulation of nonlinear fluid-structure interactions. In *Heat Transfer Summer Conference*, volume 4692, pages 243–260, 2004.

[24] R. Gordon. *Numerical simulation of vortical flows over a strake-delta wing and a close coupled delta-canard configuration*.

[25] I. Gursul, Z. Wang, and E. Vardaki. Review of flow control mechanisms of leading-edge vortices. *Progress in Aerospace Sciences*, 43(7-8):246–270, 2007.

[26] R. Hale, P. Tan, and D. Ordway. Prediction of aerodynamic loads on close-coupled canard configurations-theory and experiment. Technical report, SAGE ACTION INC ITHACA NY, 1977.

[27] W. P. Henderson. The effect of canard and vertical tails on the aerodynamic characteristics of a model with a 59 degree sweptback wing at a mach number of 0.30. *Work*, 50:9662, 1974.

[28] S. M. Hitzel and R. Osterhuber. Enhanced maneuverability of a delta-canard combat aircraft by vortex flow control. *Journal of Aircraft*, 55(3):1090–1102, 2018.

[29] R. Howard and J. J. Kersh. *Effect of canard deflection on enhanced lift for a close-coupled-canard configuration*. 1991.

[30] R. M. Howard and J. F. O'Leary. *A flowfield study of a close-coupled canard configuration*. 1993.

[31] R. M. Howard and J. F. O'Leary. Flowfield study of a close-coupled canard configuration. *Journal of Aircraft*, 31(4):908–914, 1994.

[32] D. Hummel. Documentation of separated flows for computational fluid dynamics validation. *AGARD CP 437*, 2, 1988.

[33] D. Hummel and H.-C. Oelker. Low-speed characteristics for the wing-canard configuration of the international vortex flow experiment. *Journal of aircraft*, 31(4):868–878, 1994.

[34] A. Jameson. Aerodynamic design via control theory. *Journal of scientific computing*, 3(3):233–260, 1988.

[35] A. Jameson. Optimum aerodynamic design using cfd and control theory. In *12th computational fluid dynamics conference*, page 1729, 1995.

[36] O. KANDIL and D. MOOK. A numerical technique for subsonic flows past three dimensional canard-wing configurations with edge separations. In *15th Aerospace Sciences Meeting*, page 1, 1977.

[37] H. L. Kline. *The continuous adjoint method for multi-fidelity hypersonic inlet design*. PhD thesis, Stanford University, 2017.

[38] D. W. Lacey. Aerodynamic characteristics of the close-coupled canard as applied to low-to-moderate swept wings. volume 1. transonic-supersonic speed regime. Technical report, David W Taylor Naval Ship Research and Development Center Bethesda MD, 1979.

[39] D. W. Lacey. Aerodynamic characteristics of the close-coupled canard as applied to low-to-moderate swept wings. volume 2. subsonic speed regime. Technical report, David W Taylor Naval Ship Research and Development Center Bethesda MD, 1979.

[40] D. W. Lacey. Aerodynamic characteristics of the close-coupled canard as applied to low-to-moderate swept wings. volume 3. transonic-supersonic speed regime. Technical report, David W Taylor Naval Ship Research and Development Center Bethesda MD, 1979.

[41] J. E. Lamar. Extension of leading-edge-suction analogy to wings with separated flow around the side edges at subsonic speeds. 1974.

[42] J. E. Lamar. Some recent applications of the suction analogy to vortex-lift estimates. Technical report, 1976.

[43] J. L. Lions. Optimal control of systems governed by partial differential equations. 1971.

[44] A. Lippisch. The development, design and construction of gliders and sailplanes. *The Aeronautical Journal*, 35(247):531–578, 1931.

[45] J. Longo and A. Das. Numerical simulation of vortical flows over close-coupled

canard-wing configuration. In *8th Applied Aerodynamics Conference*, page 3003, 1990.

[46] E. Malfa, L. GUARINO, and L. VISINTINI. Application of euler equations to computation of vortex flow on wing-body and close-coupled wing-body-canard configurations. In *9th Applied Aerodynamics Conference*, page 3306, 1991.

[47] F. R. Menter. Two-equation eddy-viscosity turbulence models for engineering applications. *AIAA journal*, 32(8):1598–1605, 1994.

[48] J. C. Meza. Opt++: An object-oriented class library for nonlinear optimization. 3 1994.

[49] J. J. Moré and D. J. Thuente. Line search algorithms with guaranteed sufficient decrease. *ACM Trans. Math. Softw.*, 20(3):286–307, Sept. 1994.

[50] H.-C. Oelker and D. Hummel. Investigations on the vorticity sheets of a close-coupled delta-canard configuration. *Journal of aircraft*, 26(7):657–666, 1989.

[51] F. Palacios, M. R. Colonno, A. C. Aranake, A. Campos, S. R. Copeland, T. D. Economon, A. K. Lonkar, T. W. Lukaczyk, T. W. Taylor, and J. J. Alonso. Stanford university unstructured (su2): An open-source integrated computational environment for multi-physics simulation and design. *AIAA paper*, 287, 2013.

[52] J. J. Paulson, J. L. Thomas, and M. M. Winston. *Transition Aerodynamics for Close-Coupled Wing-Canard Configuration*. AIAA, 1979.

[53] J. E. Peter and R. P. Dwight. Numerical sensitivity analysis for aerodynamic optimization: A survey of approaches. *Computers & Fluids*, 39(3):373–391, 2010.

[54] O. Pironneau. On optimum profiles in stokes flow. *Journal of Fluid Mechanics*, 59(1):117–128, 1973.

[55] O. Pironneau. On optimum design in fluid mechanics. *Journal of Fluid Mechanics*, 64(1):97–110, 1974.

[56] E. C. Polhamus. *Application of the leading-edge-suction analogy of vortex lift to the drag due to lift of sharp-edge delta wings*. National Aeronautics and Space Administration, 1968.

[57] E. C. Polhamus. Predictions of vortex-lift characteristics by a leading-edge suctionanalogy. *Journal of aircraft*, 8(4):193–199, 1971.

[58] A. Ponton, M. Lowson, and R. Barret. *The evaluation of canard couplings at high angles of attack*. 1992.

[59] Y. Qin, P. Liu, Q. Qu, and T. Hu. Wing/canard interference of a close-coupled canard configuration in static ground effect. *Aerospace Science and Technology*, 69:60–75, 2017.

[60] T. A. Rohmat, S. B. Wibowo, S. Iswahyudi, et al. Vortex dynamics study of the canard deflection angles' influence on the sukhoi su-30-like model to improve stall delays at high aoa. *Aerospace*, 6(2):12, 2019.

[61] J. Rom and R. Gordon. *High angle of attack non-linear vortex lattice calculations of canard-wing*.

[62] J. Rom, B. Melamed, and D. Almosnino. Experimental and nonlinear vortex lattice method results for variouswing-canard configurations. *Journal of aircraft*, 30(2):207–212, 1993.

[63] P. Spalart and S. Allmaras. A one-equation turbulence model for aerodynamic flows. *AIAA*, 439, 01 1992.

[64] F. Stoll and D. Koenig. *Large-scale wind-tunnel investigation of a close-coupled canard-delta-wing fighter model through high angles of attack*.

[65] E. L. TU. Effect of canard position on the longitudinal aerodynamic characteristics of a close-coupled canard-wing-body configuration. In *Astrodynamics Conference*, page 4632, 1992.

[66] E. L. Tu. Navier-stokes simulation of a close-coupled canard-wing-body configuration. *Journal of aircraft*, 29(5):830–838, 1992.

[67] E. L. Tu. Effect of canard deflection on close-coupled canard-wing-body aerodynamics. *Journal of aircraft*, 31(1):138–145, 1994.

[68] E. L. Tu. *Numerical study of steady and unsteady Canard-Wing-Body Aerodynamics*. PhD thesis, Stanford University, 1996.

[69] I. H. Tuncer and M. F. Platzer. Computational study of subsonic flow over a delta canard-wing-body configuration. *Journal of aircraft*, 35(4):554–560, 1998.

[70] F. M. White. *Viscous fluid flow*, volume 3. McGraw-Hill New York, 2006.

[71] S. B. Wibowo, B. Basuki, T. A. Rohmat, S. Siswantoro, F. Nugroho, P. Ginting, Z. Anwar, et al. Vortex dynamics study and flow visualization on aircraft model with different canard configurations. *Fluids*, 6(4):144, 2021.

[72] S. B. Wibowo, T. A. Rohmat, et al. Water tunnel flow visualization due to canard deflection effect on aircraft to improve stall delay performance. In *2018 4th International Conference on Science and Technology (ICST)*, pages 1–6. IEEE, 2018.

[73] S. B. Wibowo, S. Sutrisno, and T. A. Rohmat. Computational study of flow interactions over a close coupled canard-wing on fighter. *International Journal of Aviation, Aeronautics, and Aerospace*, 6(1):5, 2019.

[74] D. C. Wilcox. Reassessment of the scale-determining equation for advanced turbulence models. *AIAA journal*, 26(11):1299–1310, 1988.

[75] H. A. Wilson Jr and J. C. Lovell. Full-scale investigation of the maximum lift and flow characteristics of an airplane having approximately triangular plan form. Technical report, NATIONAL AERONAUTICS AND SPACE ADMINISTRATION HAMPTON VA LANGLEY RESEARCH CENTER, 1947.

[76] K. Yutuk, A. Tikenogullari, and I. H. Tuncer. Numerical investigation of vortical flows over a close-coupled delta canard-wing configuration. *Computers & Fluids*, 216:104822, 2021.